Surfaces and Interfaces 42 (2023) 103338

Contents lists available at ScienceDirect

Surfaces and Interfaces

journal homepage: www.sciencedirect.com/journal/surfaces-and-interfaces

Interface-engineered hollow carbon matrix-supported FeCo alloy as an enhanced magnetic activator for peroxymonosulfate to degrade an endocrine disruptor in water: A comparative study for elucidating advantageous roles of Fe-dopant

Tran Doan Trang [a,1], Ta Cong Khiem [a,1], Eilhann Kwon [b], Jet-Chau Wen [c], Xiaoguang Duan [d], Ha Manh Bui [e], Chechia Hu [f,*], Yiu Fai Tsang [g], Wei-Hsin Chen [h,i,j], Kun-Yi Andrew Lin [a,k,**]

[a] Department of Environmental Engineering and Innovation and Development Center of Sustainable Agriculture, National Chung Hsing University, Taichung, Taiwan
[b] Department of Earth Resources and Environmental Engineering, Hanyang University, SeongDong-Gu, Seoul, Korea
[c] National Yunlin University of Science and Technology, Douliu, Yunlin County, Taiwan
[d] School of Chemical Engineering and Advanced Materials, The University of Adelaide, SA 5005, Australia
[e] Department of Environmental Sciences, Saigon University, Ho Chi Minh 700000, Viet Nam
[f] Department of Chemical Engineering, National Taiwan University of Science and Technology, Da'an Dist., Taipei City 106, Taiwan
[g] Department of Science and Environmental Studies, The Education University of Hong Kong, Tai Po, New Territories, 999077, Hong Kong
[h] Department of Aeronautics and Astronautics, National Cheng Kung University, Tainan 701, Taiwan
[i] Research Center for Smart Sustainable Circular Economy, Tunghai University, Taichung 407, Taiwan
[j] Department of Mechanical Engineering, National Chin-Yi University of Technology, Taichung 411, Taiwan
[k] Institute of Analytical and Environmental Sciences, National Tsing Hua University, Hsinchu, Taiwan

ARTICLE INFO

Keywords:
Oxone
Sulfate radical
AOPs
MOFs
alloy

ABSTRACT

While transition metals are useful for activating peroxymonosulfate (PMS) to degrade refractory contaminants, bimetallic alloys exhibit stronger catalytic activities owing to several favorable effects. Therefore, although Co is an efficient transition metal for PMS activation, FeCo alloys are even more promising heterogeneous catalysts for PMS activation. Immobilization/embedment of FeCo (FC) alloy nanoparticles (NPs) onto carbon matrices appears as a practical strategy for evenly dispersing FeCo NPs and enhancing catalytic activities via interfacial synergies between FeCo and carbon. Herein, carbon matrix-supported FeCo alloy (CMFC) is fabricated here to exhibit a unique hollow-engineered nanostructure and the composition of FeCo alloy by using Co-ZIF as a precursor after the facile etching and Fe doping. The Fe dopant embeds FeCo alloy NPs into the hollow-structured N-doped carbon matrix, enabling CMFC to possess the higher meso-porosity, active N species as well as more superior electrochemical properties than its analogue without Fe dopants, carbon matrix-supported cobalt (CMC). Thus, CMFC exhibits a considerably larger activity than CMC and the benchmark catalyst, Co_3O_4 NP, for PMS activation to degrade bisphenol A (BA). Beside, CMFC+PMS shows an even lower E_a for BA degradation than literatures, and retains its high efficiency for eliminating BA in different water media. CMFC also maintains its composition and activities over multiple degradation cycles. The ecotoxicity assessment unravels that BA degradation by CMFC+PMS did not result in the formation of toxic and highly toxic byproducts during its decomposition process, making CMFC a promising heterogeneous catalyst for PMS activation to degrade BA.

* Corresponding author.
** Corresponding author at: Department of Environmental Engineering & Innovation and Development Center of Sustainable Agriculture, National Chung Hsing University, Taichung, Taiwan.
E-mail addresses: chechia@mail.ntust.edu.tw (C. Hu), linky@nchu.edu.tw (K.-Y.A. Lin).
[1] These authors contributed equally to this work.

https://doi.org/10.1016/j.surfin.2023.103338
Received 29 May 2023; Received in revised form 2 August 2023; Accepted 25 August 2023
Available online 26 August 2023

1. Introduction

Chemical oxidation technologies (COTs) are practical approaches for treating industrial wastewaters especially containing refractory and toxic contaminants. Conventionally, COTs involve generation of reactive oxygen species (ROS) of high-oxidation potentials for oxidizing pollutants. For instance, the Fenton's reaction would produce hydroxyl radicals (OH) for decomposing contaminants, whereas ozonation would generate $^{\bullet}OH$, superoxide ($O_2^{\bullet-}$), etc. for attacking organic pollutants. In addition, sulfate radical ($SO_4^{\bullet-}$)-based COTs also receive increasing attentions as $SO_4^{\bullet-}$ exhibits a considerably higher oxidation power of 2.5~3.1 v, and $SO_4^{\bullet-}$ would be applied under a wider range of pH with a broader selectivity and longer half-lives [1–3], making $SO_4^{\bullet-}$-based COTs are favorably adopted for treating refractory and toxic contaminants.

Nowadays, inexpensive commercial precursors of $SO_4^{\bullet-}$ are also readily available, including peroxymonosulfate (PMS), which, however, requires activation for quickly releasing $SO_4^{\bullet-}$. Among various activation methods (e.g., heat, light irradiation, ultrasound and catalysts) [4], usage of heterogeneous catalysts is acknowledged as the most promising method for activating PMS, and transition metals (e.g., Co, Fe, Mn, Ni, etc.) are useful metals for activating PMS [2,3]. While Co is validated as the most effective metal and many forms of Co-bearing materials have been extensively developed for activating PMS, recent studies have also found that bimetallic materials comprised of Co and another metal would exhibit synergistic effects for enhancing catalytic activities [5–8]. In particular, bimetallic alloys could possess even more superior features. For instance, metal alloys would possess more electron abundance which would enable metal alloys to provide more sites and higher capacity for activating PMS to degrade pollutants [9,10]. Moreover, the magnetism of metal alloys would also provide convenience for practical applications as catalysts can be easily recovered [11,12]. In addition, while metal oxides have been extensively proposed for activating PMS, studies about using metal alloys for activating PMS are still relatively few and thus, this study would attempt to propose and evaluate the metal alloys for PMS activation in order to provide more insights.

Since Fe is one of the most earth-abundant element, FeCo alloy appears as a promising catalyst for PMS activation [5,13]. For instance, Zhu et al. reported the fabrication of CoFe alloys for activating PMS to degrade emerging contaminants [14]. Nevertheless, direct usage of FeCo or other Co-bearing nanoparticles (NPs) may lead to several issues, such as easy agglomeration of NPs, difficult recover of NPs and quick deactivation [15,16]. Therefore, immobilization or embedment of FeCo alloy NPs to substrates is a practical strategy; especially, since carbon materials are highly accessible and stable, carbonaceous substrates have been adopted for supporting/embedding FeCo alloy NPs [17,18]. Moreover, carbon substrates can be even doped by hetero-atoms (e.g., nitrogen) to boost electron transfer and the catalytic activity by offering more reactive sites [19–21]. Therefore, it would be promising to develop a hybrid catalyst for embedding FeCo alloy into N-doped carbon substrates.

Even though most embedment of NPs onto carbon substrates can be achieved by post-modifications on carbon substrates, such a post-modification approach would inevitably encounter issues, such as poor dispersion of NP, easy aggregation of NP and low loading of NP [22]. Therefore, using templates containing target components (i.e., metals and organics) after direct carbonization would be an even more advantageous technique for fabricating such a hybrid catalyst. Especially, metal organic frameworks (MOFs) appear as a fascinating template owing to their coordinated structures and inclusion of metal/organics [23] and Co-ZIF would be an ideal template because the ligand of imidazolate can be transformed to N-doped carbon [24]. Through doping of Fe into Co-ZIF would also create FeCo alloy after thermal treatments. The MOF-templated method offers unique advantages for obtaining FeCo alloys, including controlled composition and structure, high purity and homogeneity, nanoscale size and morphology control, enhanced catalytic activity, facile scale-up, eco-friendliness, and potential for diverse applications. These merits make it a compelling approach for synthesizing FeCo alloys with optimized properties.

However, since Co-ZIF has polyhedral shapes and typical sizes in a few hundreds of nanometers, the resulting metal alloys resided inside the polyhedron of Co-ZIF even after carbonization would be difficultly accessed and utilized [25–27]. Therefore, herein, a facile and useful technique for making Co-ZIF a hollow structure by carving the inner portion of Co-ZIF is proposed to create a box-like hollow morphology with thin layers. After doping Fe onto such a nanobox, followed by carbonization, a thin carbon matrix-supported FeCo alloy (CMFC) would be created. Such a CMFC comprised of FeCo ally NPs embedded onto a well-defined N-doped carbon would act as a promising activator for PMS to degrade refractory pollutants.

Endocrine disruptor chemicals (EDCs) are environmental pollutants that interfere with the endocrine system. One of the most well-known EDCs is bisphenol A (BA), is widely used in the production of plastic products like epoxy and polycarbonate resins. BA can mimic estrogen, potentially causing health issues such as reproductive disorders and an increased risk of certain cancers. Various methods have been suggested for BA removal, including adsorption, filtration, advanced oxidation processes (AOPs), biological degradation, and photocatalysis. While some materials can absorb and filter BA, they only transfer the contamination from water to solid phases, and its toxicity persists. Biodegradation takes time and requires complex facilities. In contrast, chemical oxidation, such as Advanced Oxidation Processes (AOPs), proves to be an efficient and rapid approach to degrade BA from, particularly under controlled conditions and with proper catalysts [28].

BA would be then selected a representative refractory pollutant and BA degradation using PMS activated by CMFC would be studied to investigate catalytic activities of CMFC. More importantly, an analogue to CMFC without Fe dopant, carbon matrix-supported cobalt (CMC), would be also fabricated for directly comparing with CMFC for probing into the surface structure-property relationship of such hybrid materials. The corresponding degradation pathway of BA by CMFC+PMS uses both experimental analysis and computer-aided research for further investigation; the eco-toxicity evaluation of the possible intermediates would be also performed.

2. Experimental

2.1. Preparation and characterization of CMFC

The preparation process of CMFC is illustrated as displayed in Fig. 1 (a). Typically, cobalt nitrate hexahydrate (1 mmol), 2-MIM (0.05 mol) and CTAB (0.01 mmol) were consecutively added into a beaker containing 80 mL of D.I water [29]. The resulting mixture was vigorously stirred for 1 h at ambient temperature. Then, the dark-purple colored precipitate was collected by centrifugation (8000 rpm), washed thoroughly by D.I water/ethanol and dried at 65 °C for 24 h to obtain cube-like Co-ZIF. Next, a certain amount of the as-obtained Co-ZIF (i.e., 200 mg) was added into a mixture of D.I water and ethanol (ratio = 1/1 in volume) with tannic acid (i.e., 0.018 mmol) and kept stirring for 10 min to complete etching process.

The resultant material was then collected by centrifugation, washed with ethanol several times, followed by mixing with $Fe(NO_3)_3$ in N-hexane under sonication for 2 h. The Fe-doped Co-ZIF was then recovered and dried in an electric oven at 80 °C overnight, and finally carbonized in a continuous N_2 flow at 600 °C for 1 h to afford carbon-matrix-supported FeCo alloy (CMFC). For comparison, a carbon matrix-supported Co (CMC) without Fe dopant was also prepared by following the above-mentioned procedure without the mixing with Fe $(NO_3)_3$ in N-hexane.

For characterizations, the appearance of the as-prepared materials was firstly visualized by SEM and TEM (JEOL JSM-7800 F and JEM-1400, Japan). The crystalline structure of CMFC was also verified by an X-ray diffractometer (Bruker, USA). Moreover, Raman spectroscopy

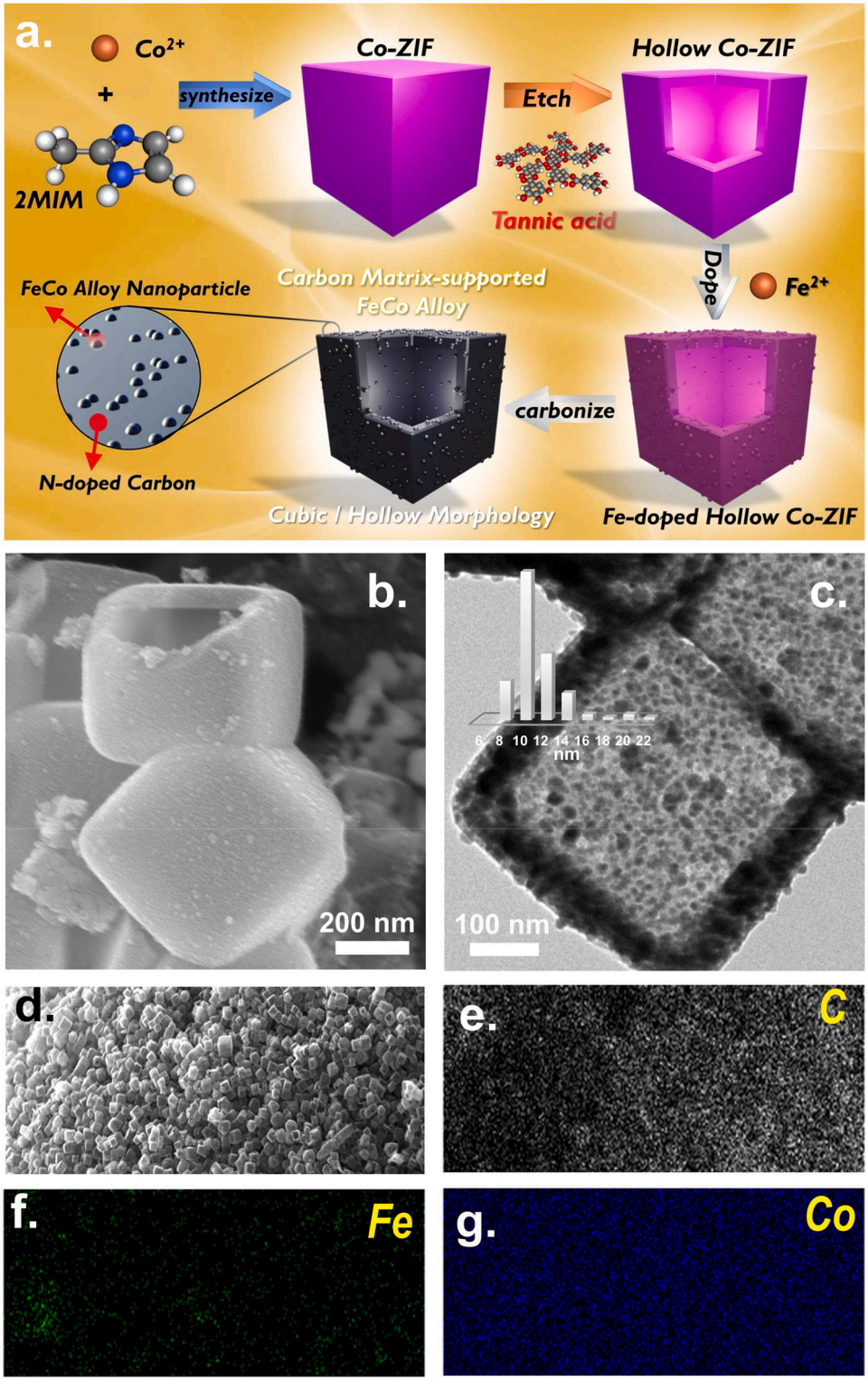

Fig. 1. (a). Preparation scheme for CMFC; (b). SEM image, (c). TEM image, (d-g). mapping analysis.

of CMFC was analyzed by a Raman spectrometer (Nanofinder 30, Tokyo Instruments, Japan). Beside, the chemical states of elements in CMFC was also characterized by X-ray photoelectron spectroscopy (XPS) (PHI 5000, ULVAC-PHI, Japan). Additionally, the physical properties of CMFC was analyzed by a volumetric analyzer (Anton Paar Auto IQ, Austria).

2.2. Catalytic activation of PMS for BA degradation

The catalytic degradation of BA by CMFC activated PMS was conducted using batch experiments. All the experiments were conducted in a dark room for eliminating the effect of energy band gap-related mechanisms. Typically, a small amount of CMFC (i.e., 100 mg/L) was firstly added into a BA solution with the initial BA concentration (C_0) of 5 mg/L for 15 min to verify whether BA might be adsorbed on CMFC

surface. Next, 150 mg/L of PMS was quickly introduced into BA solution to initiate the degradation experiment. At a fixed reaction time (t), sample aliquots were withdrawn from the BA solution, which were then filtrated by filters to separate CMFC from the solution. The remaining BA concentration of the filtrate at t (min) (C_t) was subsequently measured using high-performance liquid chromatography (HPLC) with a UV–vis detector at 298 nm. For experiments, the effects of different CMFC dosages, PMS dosages, BA initial concentrations, temperatures, initial pH values, co-existing substances and inhibitors were investigated. To explore the reactive radical species contributed to the degradation of BA by CMFC+PMS, electron paramagnetic resonance (EPR) was particularly employed using 5,5-Dimethyl-1-pyrroline N-oxide (DMPO) as a radical spin-trapping agent. The reusability of CMFC for continuous PMS activation to degrade BA was further performed by re-using CMFC to multiple BA degradation cycles. For the recycle experiments, the used CMFC was collected via centrifugation, washed thoroughly by D.I water several times before drying in an electric oven at 65 °C for 24 h, which is then employed for the subsequent degradation experiments. The intermediate products generated from BA degradation were also determined by a mass spectrometer (Thermo Finnigan Corporation, LCQ ion-trap

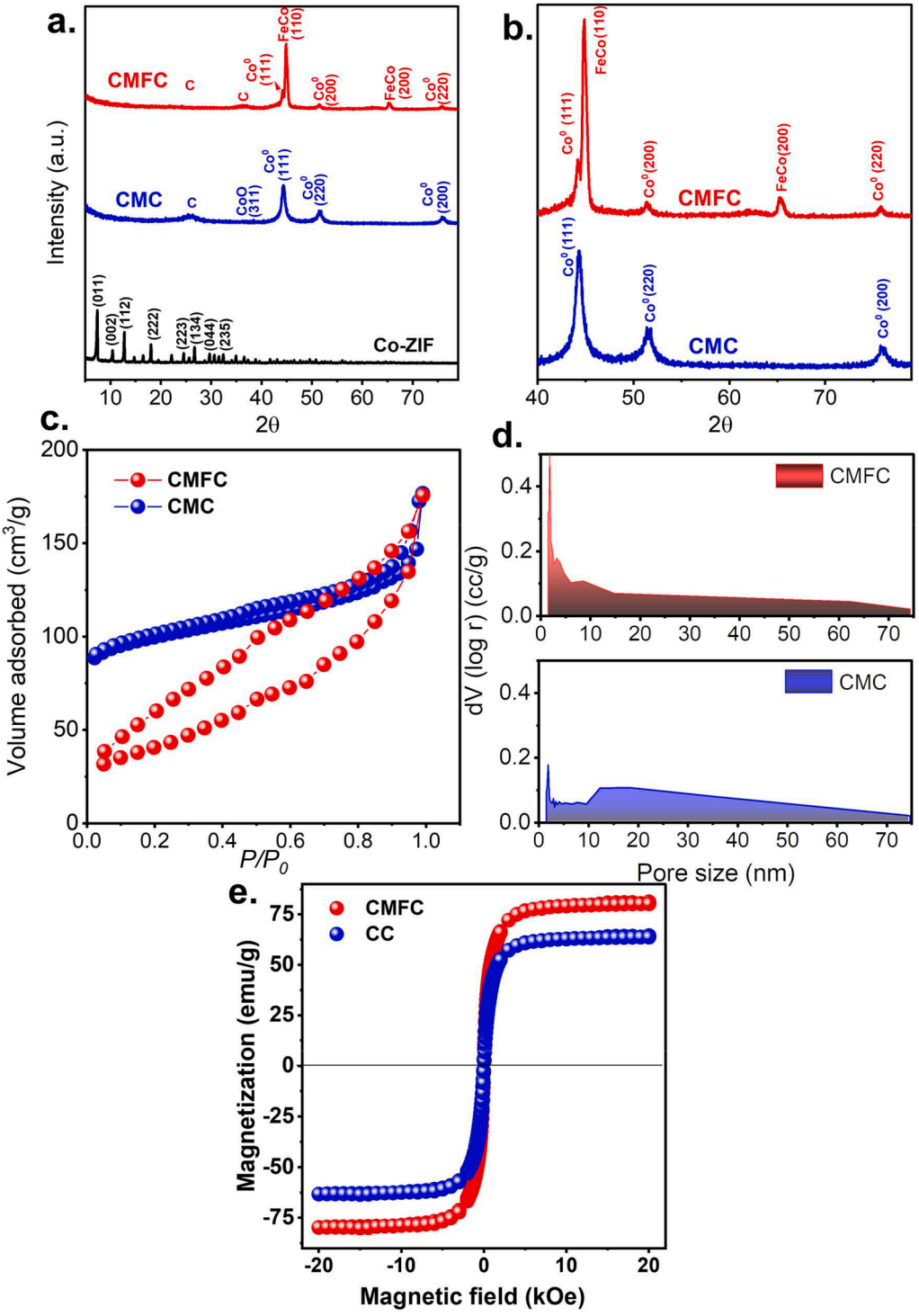

Fig. 2. (a, b). XRD patterns; (c). N_2 sorption isotherms, (d) pore size distributions of CMFC and CMC; (e) saturation magnetization of CMFC and CMC.

mass spectrometer, USA).

Moreover, as ROS might be generated during the activation and involved in BA degradation, these species were necessarily determined by electron paramagnetic resonance (EPR) using 5,5-Dimethyl-1-pyrroline N-oxide (DMPO) and 2,2,6,6-tetramethylpiperidine (TEMP) as radical spin-trapping agents to reveal the mechanism of BA degradation. Beside, the intermediates derived from BA degradation were also determined using a mass spectrometer (Thermo Finnigan Corporation, mass spectrometer, USA). For $O_2^{\bullet-}$, as the consumption of nitro blue tetrazolium (NBT) is correlated to the generation of $O_2^{\bullet-}$, NBT was used as a probe to quantify $O_2^{\bullet-}$. The sample aliquots were analyzed with an UV–Vis spectrophotometer (CT-2200, Chrom Tech) [30]. Degradation products of BA were then identified by liquid chromatography-mass spectrometry-mass spectrometry (Thermo TSQ Quantum, USA). Metal concentrations in solutions were analyzed using ICP-MS (Inductively coupled plasma mass spectrometer) (PerkinElem Elan, USA). The preparation of CMFC was implemented as shown in Fig. 1(a) and the detailed fabrication process, BA degradation by PMS, analytic procedures, and computational chemistry are provided in the supplementary material.

For quantifying the degradation kinetics, the pseudo-first-order rate law would be employed to quantify the observed rate constant, *k*, as follows [31–34]:

$$\mathrm{Ln}(C_t / C_0) = -kt \quad (1)$$

3. Results and discussion

3.1. Properties of CMFC

3.1.1. Morphologies and compositional analyses

As CMFC was derived from Co-ZIF, the morphology of Co-ZIF was firstly determined as shown in Fig. S1(a), in which nanoscale cubes with clear faces and well-defined edges were observed. In this process, 2-MIN and Co ion formed Co-ZIF by coordinate bond. The CTAB as a surfactant induced Co-ZIF to form a cube. The transmission image of Co-ZIF (Fig. S1(b)) also demonstrates that the pristine Co-ZIF was cubic and solid. Moreover, Fig. 2(a) further indicates that the XRD pattern of pristine Co-ZIF was well-indexed to the reported pattern [26,27,35], demonstrating that ZIF has been formed.

Through the post treatment with tannic acid and doping with Fe^{2+}, followed by carbonization, the resulting product (Fig. 1(b)) still exhibited the cubic morphology; however, the faces of the resultant product were obviously roughened and decorated with numerous fine nanoparticles (NPs). More importantly, the original solid structure had been changed to the hollow structure with very thin outer layers as observed through the fractures. The corresponding transmission image (Fig. 1(c)) further validated that the solid texture of pristine Co-ZIF had disappeared and transformed to the hollow texture and thickness of outer layers was ca. 80∼100 nanometers.

The hollow structure was caused by tannic acid, a common organic acidic compound. The tannic acid with plenty single bond OH groups, liberating free proton (H^+) to break the characteristic Co-N bonds. Meanwhile, new N-H bonds and coordinated Co-TA complex can be formed, converting the Co-ZIF coordination framework into a coordination network between Co^{2+} ions and tannic acid. Those tannic acid and partial Co-TA coordination compounds can easily attach on the surface, relieving the collapses of shell parts. Then, the hollow structure was formed by the continuous etching and re-coordination. During this step, the tannic acid shell remains intact, acting as a protective layer around the void left by the removed core material. When Fe is impregnated, C-Fe and Co-Fe bonds can be formed, trapping Fe more effectively by chemical adsorption.

Moreover, the closer-view in Fig. 1(c) further reveals that the outer layers of the resultant product were actually assembled by numerous NPs exhibiting sizes in the range of 6–22 nm as seen in the inset. Its corresponding XRD pattern was then measured in Fig. 2(a), which exhibited a different pattern, demonstrating that Co-ZIF had been transferred to another material through the etching, doping and carbonization. A few peaks were noted on 36.7°, 44.2°, 44.9°, 51.4°, 65.2° and 75.8°. While the peak at 36.7° was ascribed to carbon (JCPDS Card# 50-0927), the dominant peaks at 44.9° and 65.2° were attributed to FeCo alloy (JCPDS Card# 65-6829), whereas the minor peaks at 51.4° and 75.8° were derived from Co^0 (JCPDS Card# 15-0806). The presence of these species further confirmed that Fe was successfully doped into the resultant product and the pristine

Co-ZIF had been changed to a hybrid material comprised of carbon, Co^0 and, more importantly, FeCo alloy. The carbon was derived from carbonization of the organic component, whereas FeCo alloy and Co^0 were afforded from thermal synthesis of Fe and Co ions under an oxygen-lean condition, formulating the carbon matrix-supported FeCo alloy (CMFC).

Fig. 1(d) further displays the mapping analysis of CMFC nanocubes, which reveals the uniform distribution of carbon, Fe and Co all over these CMFC nanocubes, validating that the etching, and Fe doping were homogeneously applied on Co-ZIF nanocubes during the preparation process.

On the other hand, an analogue to CMFC was also prepared without the doping of Fe^{2+}. As shown in Fig. S2(a, b), even without the Fe^{2+} doping, the etching and carbonization treatment has also successfully converted Co-ZIF to the hollow-structured material. The corresponding transmission image further confirmed unraveled that the faces of the resulting product (without the Fe2+ doping) also contained many fine NPs on its surfaces but the sizes of these NPs seemed much smaller. Fig. 1 (b) also displays its XRD pattern which was also different than Co-ZIF with a series of notable peaks at 26.3°, 44.2°, 51.6° and 76.1°. Specifically, the signal on 26.3° could be attributed to carbon owing to carbonization of organic molecules, while other peaks were ascribed to Co^0 (JCPDS Card# 15-0806), formulating the carbon matrix-supported Co (CMC).

These comparisons further reveal that CMFC seemed to contain the relatively large NPs in contrast to CMC possibly because the Fe^{2+} was doped and inserted into the coordination and caused disturbance to the Co-coordinated structure.

3.1.2. Textural properties

As CMFC exhibited a unique hollow structure with the composition of NPs, its textural property was then further analyzed in Fig. 2(c), and the adsorption curve could be classified as a type IV adsorption accompanied by a noticeable hysteresis, suggesting that CMFC was porous, especially mesoporous. The large hysteresis also suggested that the pore structures in CMFC was more complex possibly because differently-sized NPs of FeCo alloy were embedded into the carbon matrix, creating variously-sized pores. The presence of mesopores is confirmed by its pore distribution (Fig. 2(d)), which ranges from 2 to 75 nm. The relatively high N_2 sorption also enabled CMFC to show a high surface area as 145 m^2/g and its pore volume was determined as 0.21 cc/g.

The adsorption curve of CMC was measured in Fig. 2(c). Even though a relatively high N^2 sorption was achieved, the corresponding hysteresis loop was much smaller due to its relatively homogeneous pore sizes of NPs. Therefore, while the surface area of CMC would be 313 m^2/g, its pore volume was merely 0.13 cc/g, which was much lower than that of CMFC.

Since CMFC was consisted of FeCo alloy and metallic Co, it has magnetic characteristics and hence it might be intriguing to explore the magnetic features of the CMFC. In Fig. 2(e), CMFC displayed a significant magnetization, and its saturation magnetization reached 81 emu/g, which was significantly higher than that of CMC as 63 emu/g. The mixture of FeCo alloy and metallic Co species allowed CMFC to manifest powerful magnetization, rendering it a material that can be readily recovered.

3.2. Degradation of BA by CMFC+PMS system

BA elmination using PMS activated by CMFC was evaluated in Fig. 3 (a). Nevertheless, since it was possible that BA might be removed via adsorption, the adsorption of BA onto CMFC was investigated. In Fig. 3 (a), the BA concentration was almost no change in the presence of CMFC, signifying that BA could not be eliminated by adsorption. Once PMS alone was used, BA was only marginally eliminated in 30 min, demonstrating that PMS without activation could not adequately destroy BA. However, when both of CMFC and PMS were combined, BA concentration was quickly reduced and fully removed in 30 min, suggesting that CMFC could activate PMS to eliminate BA in water. For comparison, traditional Co_3O_4 NP (Fig. S3) and CMC were also adopted to decompose PMS for eliminating BA in Fig. 3(a). Co_3O_4 NP+PMS enabled C_t/C_0 in 30 min to reach 0.68 (i.e., 32% of BA was removed), whereas CMC+PMS led to $C_t/C_0 = 0.5$ in 30 min. These cobaltic catalysts were ascertained for decomposing PMS to degrade BA; however, BA degradation efficiencies of Co_3O_4 NP and CMC seemed noticeably lower than that of CMFC.

To further quantitatively compare performances of these catalysts for BA degradation, the pseudo 1st order equation was then employed and the corresponding rate constants of BA degradation are summarized in Fig. 3(b). The rate constant (k) by CMFC+PMS would be 0.037 min^{-1}, larger than the rate constants of Co_3O_4 NP+PMS (0.004 min^{-1}) as well as CMC+PMS (0.017 min^{-1}), confirming advantage of CMFC over Co_3O_4 NP and CMC.

In view of the much faster BA degradation by CMFC, it would be interesting to further probe into PMS consumption by CMFC in comparison with other catalysts. Thus, the variation of PMS concentration during BA degradation was then analyzed in Fig. 3(c). The PMS concentration with CMFC decreased rapidly during BA degradation as ~70% of PMS had been decomposed by CMFC in 120 min. On the contrary, the PMS consumption during BA degradation by CMC seemed much less (~48%) and slower. The rate constants of PMS consumption by these catalysts are displayed in Fig. 3(d) and the k using CMFC was determined as 0.015 min^{-1}, while the rate constant by CMC would be much smaller as 0.008 min^{-1} and that by Co_3O_4 NP was 0.002 min^{-1}, validating that the PMS consumption by CMFC seemed much more effective and faster than CMC and Co_3O_4 NP, thereby enabling the faster BA degradation. The limited catalytic capacity of CMC and commercial Co_3O_4 is due to its low surface area because of serious aggregation as shown in Fig. S3, thereby reducing the number of active sites available for catalysis. Beside, the high crystallinity of the commercial Co_3O_4 might also lead to fewer defects and reactive sites on the surface.

Since activating PMS would be associated with surficial reactions of PMS and catalysts, surface chemistry of catalysts shall offer crucial contributions to PMS activation [36]. As CMFC exhibited a noticeably higher catalytic activity for PMS activation, it would be insightful to

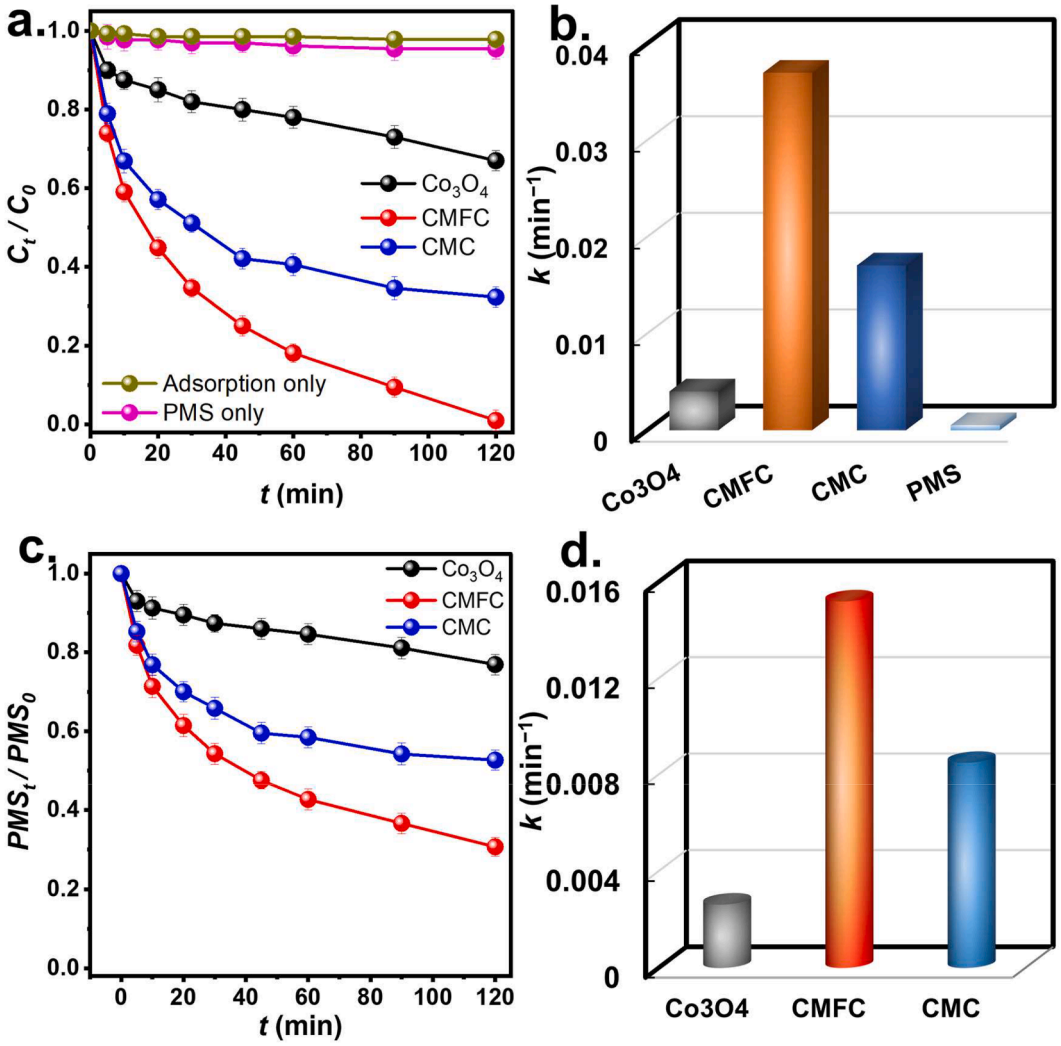

Fig. 3. (a) Comparison of degradation of BA and (b) corresponding rate constants of BA degradation; (c) comparison of PMS consumption and (d) rate constants of PMS consumption (Catalyst = 200 mg/L, PMS = 200 mg/L, T = 30 °C).

examine surficial chemistry of these catalysts for comparisons. Herein, X-ray photoelectron spectroscopy analyses of CMFC and CMC were performed as shown in Fig. 4. Specifically, the C1s curve of CMFC (Fig. 4 (a)) would be resolved to multiple bands at 284.0 eV, 286.6 eV and 288.5 eV, corresponding to the C-C, C-N, and C=O groups [37]. The Co2p band of CMFC would be also obtained and resolved to multiple bands (Fig. 4(b)). Particularly, the band on 778.6 eV would be attributed to Co0, whereas other bands at 780.4 and 796.3 eV would correlate to Co^{2+} species [38].

Moreover, the Fe2p curve (Fig. 4(c)) would be analyzed to display multiple bands, and the band at 705.8 eV corresponds to Fe^0 in FeCo [39]; 710.2, 713.4, and 723.3 eV could be Fe^{2+} and Fe^{3+} species as FeCo NPs might be oxidized upon the contact with oxygen. Additionally, N1s in CMFC would be revealed in Fig. 4(d), showing multiple bands on

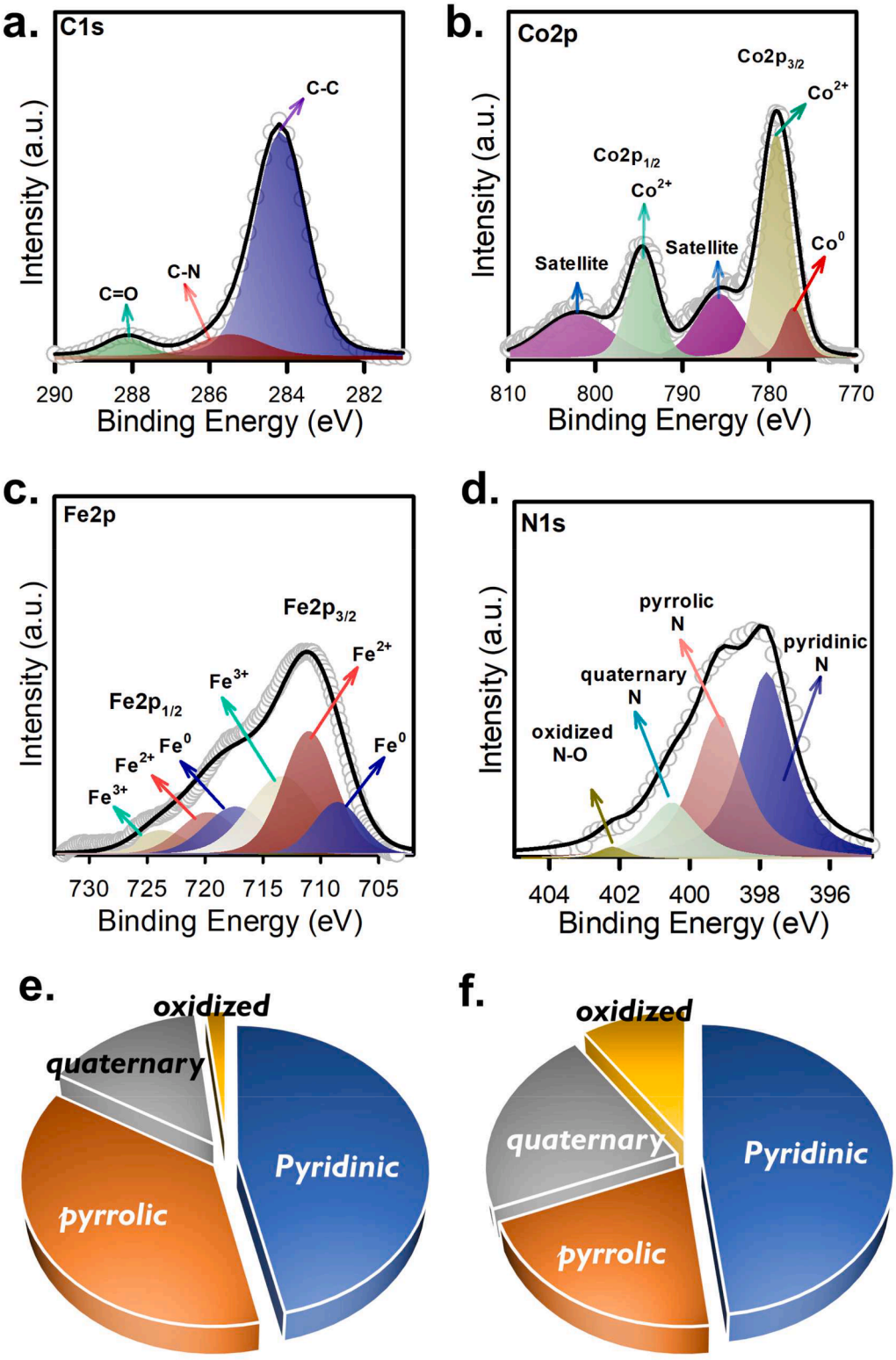

Fig. 4. (a–d). XPS analyses of CMFC; (e). fractions of N species in CMFC; and (f). fraction of N species in CMC.

398.3, 399.3, 400.5 and 402.5 eV, ascribing to the pyridinic N, pyrrolic N, quaternary N and N-O group [40].

For comparisons, the XPS analysis of CMC was also performed as shown in Fig. S4. The C1s band was analyzed to reveal a series bands corresponding to C-C, C-N, and C=O [37]. Additionally, the band on 778.5 eV was derived from Co^0, whereas other bands on 780.2 as well as 796.3 eV corresponded to Co^{2+} species [38]. The N1s band also contained multiple bands on 398.3, 399.3, 400.5 and 402.5 eV, ascribing to pyridinic N, pyrrolic N, quaternary N and N-O group [40].

While CMFC and CMC consisted of Co species, CMFC consisted of Fe^0, Fe^{2+} and Fe^{3+}, which would serve as additional reactive sites for activating PMS. Previous studies have reported that dual or multiple-metallic compositions would afford more reactive sites for mediating PMS activation, thereby enhancing catalytic activities [12,41]. CFMC also exhibited a different pattern for nitrogenous species, with pyridinic N, pyrrolic N, and quaternary N contributing 46%, 37%, and 24%, respectively, while CMC was comprised of pyridinic N, pyrrolic N, quaternary N as 54%, 23%, and 24%. Because both pyridinic N and pyrrolic N have been verified as active sites for PMS activation [42], the combined amount of pyridinic N and pyrrolic N in CMFC (i.e., 83%) was significantly greater than the amount in CMC (77%). The comparatively large pyridinic and pyrrolic N fractions in CMFC were projected to allow CMFC to have many more active sites than CMC, resulting in CMFC having greater activities for activating PMS in BA decomposition.

In addition to XPS analyses, Raman spectroscopy was also employed to investigate molecular differences between CMFC and CMC via unraveling structural fingerprints. Fig. 5(a) displays Raman spectra of CMFC, and CMC, and all of these were comprised of similar patterns with noticeable peaks at 192, 474, as well as 680 cm^{-1}, attributed to the F_{2g}, E_g, as well as A_{1g} of Raman active vibration modes in Co metal species [43]. While these results confirm that CMFC and CMC both consisted of Co, the zoom-in views of these bands reveal noticeable differences. For instance, Fig. 5(b) further displays that the A_{1g} band of CMC centered at 673 cm^{-1}; however, the center of the band in CFMC had switched from 673 cm^{-1} to 668 cm^{-1}. The similar band shift had been also observed in the case of F_{2g} as shown in Fig. 5(c). As the band center of CMC was at 191 cm^{-1}, the F_{2g} band center of CMFC shifted to the lower location to 186 cm. Since A_{1g} and F_{2g} could be ascribed to the coordination of Co species, these shifts suggest that CFMC contains defective sites or oxygen vacancies [44]. This feature might enable CMFC to reveal more catalytic active surfaces [44], that would possibly improve catalytic activities of PMS activation.

Moreover, two additional bands resided on 1331 cm^{-1} and 1587 cm^{-1} might correspond to the D and G band of the carbon matrices in CMFC and CMC. The intensities of D and G bands signify extents of defect and graphitization in catalysts [45,46]. The carbonaceous matrix in CMFC (Fig. 5(d)) was then found to contain a higher degree of defect than that in CMC. As the carbonaceous defect has been also reported as

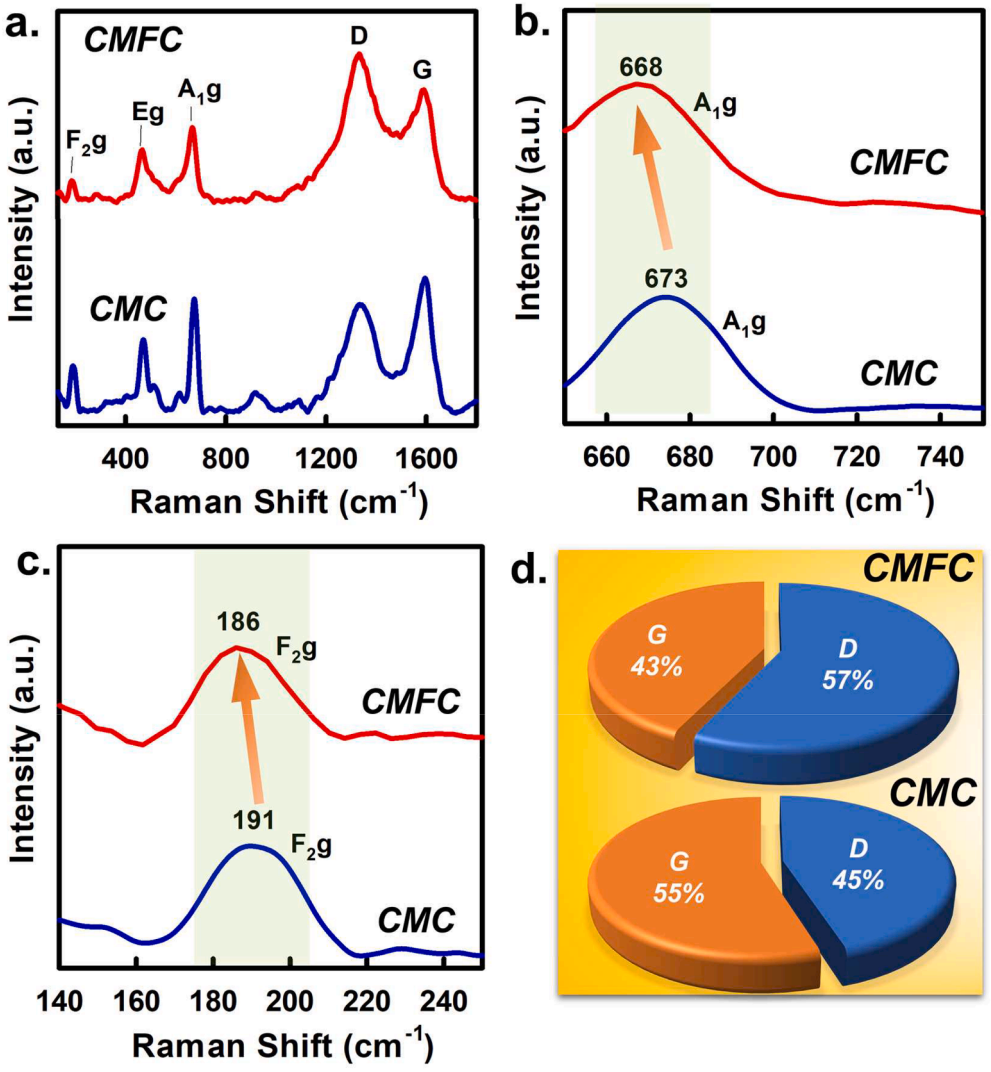

Fig. 5. (a). Full-survey Raman spectra of CMFC and CMC; (b-c), regional Raman spectra of CMFC and CMC; and (d) fractions of G and D bands in CMFC and CMC.

possible active sites for PMS activation, the higher fraction of D band in CMFC might be also the reason for enabling CMFC to exhibit higher catalytic activities [47].

On the other hand, PMS activation would also involve reduction-oxidation reactions in PMS and activators; thus, electro-chemistry of catalysts shall also offer crucial contribution to PMS activation [36]. As CMFC exhibited a considerably larger activity than CMC in BA degradation, it was informative to examine electrochemical differences between CMFC and CMC. Fig. 6(a) firstly reveals cyclic voltammetry (CV) curves of CMFC and CMC; CMC displayed a relatively small CV curve with less noticeable redox peaks in this potential window, whereas CMFC obviously showed a larger CV curve with notable redox peaks. Accordingly, CMFC exhibited an essentially higher specific capacitance as 19.0 F/g than 3.3 F/g in CMC, validating that CMFC revealed much more superior redox properties and would lead to faster inter-facial processes than CMC [48]. Furthermore, the linear sweep voltammograms (LSV) curves of CMFC would be also determined in Fig. 6(b). On the level of 5 μA, a starting potential of 0.70 V must be achieved by CMFC, while CMC required a slightly higher starting potential of 0.82 V, demonstrating that the electronic transportation in CMFC seemed more effective than in CMC. Moreover, the charge transfers in both of catalysts were also analyzed via their Nyquist plots (Fig. 6(e)). In comparison to CMC, CMFC showed a considerably more narrow semi-circle at the high-frequency region, indicating that CMFC contained a larger-degree charge transfer and a smaller resistancy than CMC [49]. These analyses demonstrated that CMFC with the more superior porous properties and more active surfaces would further enable CMFC to possess more advantageous electrochemical behaviors that made CMFC show the considerably higher catalytic activity for PMS activation to degrade BA.

3.2.1. EIS Nyquist plots

Additionally, the difference between CMFC and CMC was further unveiled by looking into interactions of PMS with active sites of CMFC and CMC. Therefore, the computation-aided investigation was adopted on the basis of the First-Principles simulation for distinguishing essential reactions (i.e., adsorption) between PMS and FeCo alloy in CMFC and Co in CMC, respectively. In particular, the geometrically-optimized (110) dominant plane of FeCo alloy in CMFC would be demonstrated as a surface plane of FeCo, whereas the geometrically-optimized (111) dominant plane of Co in CMC would be adopted as the surface of Co as illustrated in Fig. 7. The adsorption energy of PMS to the catalyst surface was quantified using the following equation:

$$\text{Adsorption energy}(E_{ad}) = E_{PMS@catalyst} - E_{PMS} - E_{catalyst}$$

The corresponding E_{ad} of PMS to FeCo alloy at the (110) plane would be calculated as -1.66 eV, whereas E_{ad} of PMS to Co alloy at the (111) plane was -1.19 eV. As the both cases of E_{ad} were negative, PMS was validated to favorably adsorbed to these metallic surfaces. However, the more negative E_{ad} in the case of FeCo alloy suggested that the adsorption process of PMS to CMFC might be more favorable than that to CMC. Such a difference might be also a factor for making CMFC exhibit the higher catalytic activity of PMS activation than CMC. Discussion of other effects (PMS and catalyst dosages) on BA degradation can be found in the supplementary material (Fig. S5).

3.3. Other factors on degradation of BA by CMFC+PMS system

Since CMFC+PMS was capable of eliminating BA from water, it was essential to investigate other factors on BA degradation, such as temperature and pH. Fig. 8(a) displays BA elimination by CMFC+PMS at 30 to 50 °C. At 40 °C, BA elimination could proceed much faster as the corresponding rate constant rose up from 0.037 min^{-1} to 0.054 min^{-1}. Once the temperature further rose to 50 °C, BA degradation proceeded even faster and its k was raised up to 0.067 min^{-1}, demonstrating the positive effect of higher temperatures on BA elimination possibly owing to the promoted mass transfer at high temperatures. This phenomenon occurs because higher temperatures generally enhance the reaction kinetics by providing more energy to the reacting molecules, leading to a higher frequency of successful collisions and increased formation of reactive species.

Since Bisphenol A (BA) is focused in this study and BA is one of the well-known EDCs, it would be meaningful and insightful to further compare degradation efficiencies of BA using other sulfate radical-based processes/techniques to reveal competitiveness of the proposed catalyst, CMFC.

For instance, Choi et al. proposed hydrodynamic cavitation and activated persulfate for degrading BA, and found that both hydroxyl and sulfate radicals contributed to BA degradation [50]. On the other hand, Olmez-Hanci et al. and Chauch et al. reported that the heat-activated persulfate was useful for removal of BA from contaminated water [51, 52]. Furthermore, Yan et al. also proposed to employed powdered iron to activate persulfate to degrade BA and found that the degradation of BA followed the pseudo first order rate law [53]. Similarly, many other heterogeneous catalysts were also employed (e.g., CoMnAl and metal-free carbon catalysts) for activating PMS to degrade BA [28].

For further comparisons CMFC and these other processes and techniques for BA degradation, their corresponding activation energies of BA were also calculated using the following equation by the k values at different temperatures were modeled via the following law:

$$\ln k = \ln A - \frac{E_a}{RT} \quad (2)$$

the corresponding E_a would be determined as 20.7 kJ/mol, which surpassed many Ea values of BA degrading by sulfate-radical-based COTs (Table S1), displaying that CMFC would be a certainly competitive activator for PMS to eliminate BA.

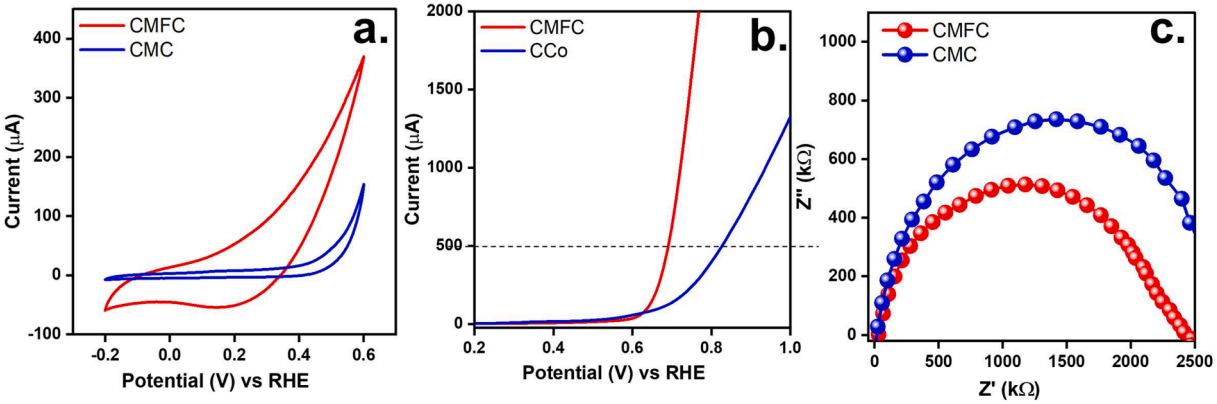

Fig. 6. Electrochemical properties of CMFC and CMC: (a) CV curves, (b) LSV curves.

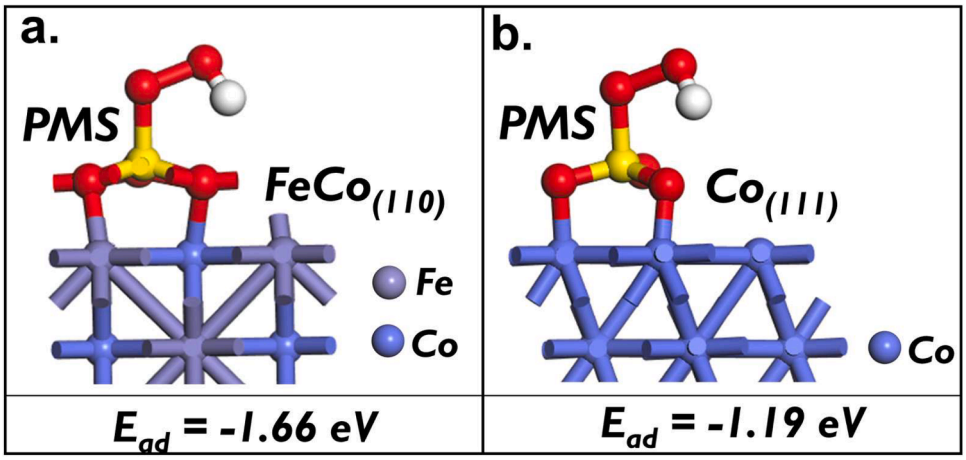

Fig. 7. DFT calculation: (a) adsorption of PMS to FeCo alloy (110), and (b) adsorption of PMS to Co (111).

The influence of pH to BA elimination by CMFC+PMS would be examined in Fig. 8(b). At pH = 7, the neutral condition, it enabled the rapid BA elimination, a relatively acidic condition at pH = 5 caused a slightly slower BA degradation as the k dropped to 0.021 min^{-1}. Once the initial condition was more acidic at pH = 3, the BA degradation was further slowed with a slower k as 0.005 min^{-1}. Such a favorable effect under the acidic condition might be because the relatively high concentration of H^+ in the acidic environment can interact with the $SO_4^{\bullet-}$ as well as $^{\bullet}OH$ to "spend" these radicals through the following equations [54,55]:

$$H^+ + SO_4^{\bullet-} + e^- \rightarrow HSO_4^- \quad (3)$$

$$H^+ + {}^{\bullet}OH + e^- \rightarrow H_2O \quad (4)$$

Therefore, fewer radicals would be present under the acidic condition for degrading BA, leading to the less efficient BA degradation. In addition, PMS itself would be more indolent under the acidic condition [56], thereby causing PMS much harder to activate and then leading to the less efficient BA degradation.

As the starting pH was 9, the alkaline condition, BA degradation was noticeably affected as BA degradation proceeded slowly with a k = 0.012 min^{-1}. When pH changed to 11, the BA degradation was further slowed with a k = 0.001 min^{-1}. The data also demonstrate that the alkaline condition seemed slightly unfavorable to BA degradation by CMFC+PMS possibly because the CMFC surface might grow even more negatively-charged in the basic environment (Fig. S6), causing a stronger repulsion between BA, CMFC as well as SO_5^{2-} and constraining production of radicals [57]. Beside, since the *p*Ka of PMS is 9.4, and the highly basic condition would make the electrostatic repulsion even more intensive, thereby constraining the reaction between PMS and CMFC [56].

Further evaluation of BA decomposition by CMFC+PMS in various water environments would be also informative. Tap water and seawater comprising BA were employed as the testing media in Fig. 6(d), alongside DI water. Notably, when tap water was applied, the beginning of BA degradation was still highly efficient with a rate constant of k = 0.030 min^{-1}. Since tap water contains numerous substances, including ions and solids, the overall BA degradation efficacy was satisfactory, as > 90% of BA was eliminated within 120 min. BA could still be degraded by CMFC+PMS in seawater, despite the slightly reduced k value of 0.020 min^{-1}, because seawater comprises a substantial amount of impurities, particularly ions and minerals.

It is possible that Cl is present in seawater and tap water, which contributes to their less efficient degradation because Cl^- might react $SO_4^{\bullet-}$ to afford chloride radicals (i.e., $Cl^{\bullet}$, $Cl_2^{\bullet-}$) [58], that show smaller oxidation power than $SO_4^{\bullet-}$; therefore, the BA elimination efficacy decreased. In spite of this, CMFC+PMS was still an effective and practicable method for degrading BA in both potable water and seawater.

3.4. Recyclability of CMFC for BA elimination

As CMFC activated PMS to efficiently BA, the recyclability of CMFC to eliminate PMS over multiple cycles was then investigated. Fig. 8(f) displays that BA was capable of degrading BA over 5 continuous cycles without considerable changes by the spent CMFC. This result indicates that the spent CMFC remained stable and useful to activate PMS for degrading BA. The leaching Fe and Co from CMFC from the end of the recyclability test were then measured using Inductively Coupled Plasma Mass Spectrometry. After the consecutive 5 cycles, the concentrations of Fe and Co ions were measured as 0.3 and 0.7 mg/L (Table S2), that were much less than the catalyst dosage as 200 mg/L. The XRD pattern of the spent CMFC was also analyzed in Fig. S7 and the pattern was comparable to that of the pristine CMFC. In addition, the TEM image of the used CMFC was also measured and displayed in Fig. S8, which was also highly comparable to the pristine CMFC without significant destruction. These results suggest that CMFC was a stable and durable heterogeneous catalyst.

3.5. Degradation mechanism by CMFC+PMS

To further realize types of ROS involved during BA degradation, a series of probe agents would be then examined. Tert-butanol (TBA) would be adopted as a probe agent for $^{\bullet}OH$, whereas methanol can be used for probing the presence of $SO_4^{\bullet-}$ and $^{\bullet}OH$. Fig. 9(a) displays that when TBA was introduced, BA degradation proceeded slightly slower and its corresponding rate constant decreased from 0.037 to 0.018 min^{-1}, signifying that $^{\bullet}OH$ shall be present and contribute to BA degradation. When methanol was then introduced, the BA degradation seemed to inhibited seriously as its k would be merely 0.002 min^{-1}, suggesting that $SO_4^{\bullet-}$ and $^{\bullet}OH$ would simultaneously co-exist during BA degradation. Beside, another probe agent, benzoquinone (BQ), was employed to determine the existence of superoxide ($O_2^{\bullet-}$). Fig. 9(b) displays that the presence of BQ also caused BA degradation to proceed much slowly with a k = 0.021 min^{-1}, possibly suggesting that $O_2^{\bullet-}$ might also appear during BA degradation. Additionally, another probe agent, NaN_3, was then adopted to investigate the presence of the non-radical species, singlet oxygen ($^1O_2$), and the introduction of NaN_3 also made BA degradation proceed relatively slowly with a k = 0.011 min^{-1}, signifying that $^1O_2$ also possibly occurred from CMFC+PMS during BA degradation, which was involved the non-radical decomposition pathway.

To investigate the existence of such ROS more thoroughly, the formation of $SO_4^{\bullet-}$ and $^{\bullet}OH$ at various intervals would be estimated via

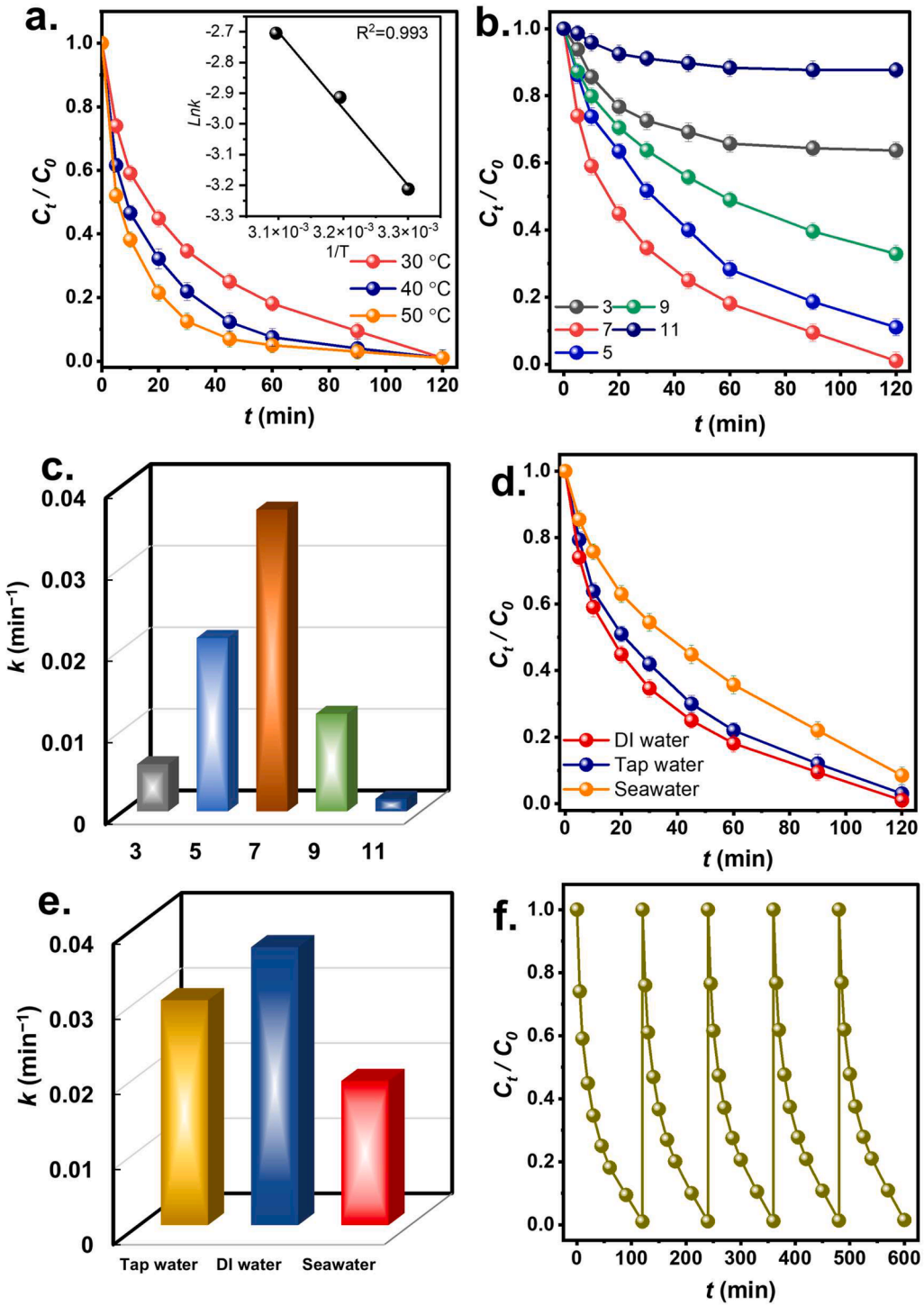

Fig. 8. Effects of various factors on BA degradation by CMFC+PMS: (a) temperature, (b,c) pH and corresponding rate constants, (d, e) scavengers and corresponding rate constants; (f) recyclability.

"semi-quantitative" investigations employing specific probe agents [59–61]. As shown in Fig. 9(c), the appearance of SO4•– and •OH was confirmed by the formation of para-benzoquinone (*p*-BQ) and para-hydroxybenzoic acid (*p*-HPA), indicating that the concentrations of $SO_4^{\bullet-}$ and •OH increased over time. However, the quantity of $SO_4^{\bullet-}$ appeared to be greater than that of OH, which was consistent with what was observed in scavenger experiments.

In addition, the production of $^1O_2$ could be determined by linking it to the furfuryl alcohol (FFA) consumed during the reaction with $^1O_2$ ($k = 1.2 \times 10^8\ M^{-1}s^{-1}$) [62,63]. Fig. 5(e) depicts the FFA consumption at various reaction periods for PMS alone and CMFC+PMS. One can observe that PMS without CMFC would result in marginal production of $^1O_2$. However, CMFC+PMS would accelerate the consumption of FFA, corroborating that CMFC would lead to the decomposition of PMS and initiate the generation of 1O2 for the nonradical destruction of BA.

To determine actual species of ROS from CMFC+PMS during BA degradation, electron paramagnetic resonance (EPR) would be subsequently employed by using 5,5-Dimethyl-1-pyrroline N-oxide (DMPO) and 2,2,6,6-tetramethylpiperidine (TEMP) as spin-trapping agents. Fig. 10(a) reveals that when DMPO was introduced in the absence of

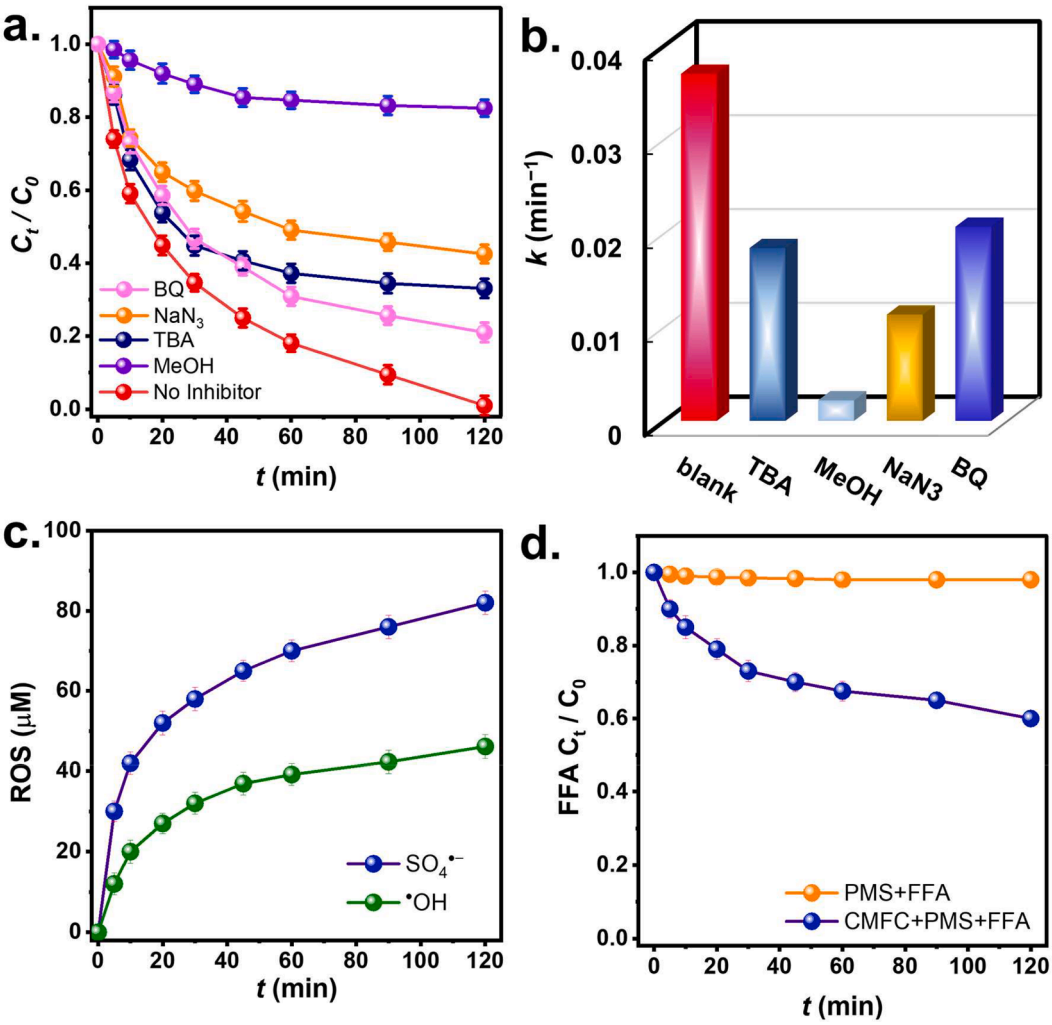

Fig. 9. (a) Effects of various scavengers and (b) corresponding rate constants; (c) concentrations of ROS; and (d) FFA consumption by CMFC+PMS.

CMFC, no obvious pattern was observed. Nevertheless, as DMPO, PMS and CMFC were present simultaneously, a distinct pattern was then observed and attributed to DMPO-SO4 and DMPO-OH as indicated in Fig. 10(a). This ascertains that both $SO_4^{\bullet-}$ and $^{\bullet}OH$ could form by PMS+CMFC, contributing to BA degradation. Moreover, the same measurement was then performed in methanol to examine whether the superoxide, $O_2^{\bullet-}$, would be produced from CMFC+PMS. While insignificant signal was observed in the case of DMPO and PMS in methanol, a notable signal could be detected in the case of DMPO, PMS and CMFC in methanol (Fig. 10(b)). However, the signal was considered as DMPO-X because of oxidation of DMPO rather than the signal of $O_2^{\bullet-}$, suggesting that no significant amount of $O_2^{\bullet-}$ was present during BA degradation. To evaluate the existence of $O_2^{\bullet-}$, another analytic technique by using nitro blue tetrazolium (NBT) was employed as NBT would be oxidized specifically by $O_2^{\bullet-}$ to monoformazan, absorbing the visible light at 530 nm. Nonetheless, Fig. 10(d) displays that when NBT was introduced to BA degradation, the spectral variation did not show noticeable bands at 530 nm, indicating insignificant existence of $O_2^{\bullet-}$.

In the earlier section, we observed that the introduction of BQ slightly inhibited BA degradation. This phenomenon has been also observed in literatures because when $O_2^{\bullet-}$ was insignificant, the addition of BQ might consume a part of PMS without generating ROS, thereby intervening with BA degradation [64]. These analyses also corroborated that BA degradation by CMFC+PMS was certainly involved with a series of ROS ($SO_4^{\bullet-}$, $^{\bullet}OH$, $^1O_2$) as depicted in Fig. 10(e).

3.6. Degradation pathway of BA by CMFC and PMS

Since CMFC can efficiently activated PMS to degrade BA, it was important to further investigate the BA elimination route. For exploring the BA degradation pathway by ROS, the computational chemistry using the Density Function Theory (DFT) was adopted to investigate the molecular susceptibility in BA. The molecular structure of BA was be geometrically-optimized as shown in Fig. 11(a). Accordingly, Fig. 11(b) and (c) displays the highest occupied molecular orbital (HOMO) and the lowest unoccupied molecular orbital (LUMO) of BA. In general, the HOMO regions would attract electrophilic attacks, and both $SO_4^{\bullet-}$ and $^{\bullet}OH$ are considered to exhibit electrophilic nature and $^1O_2$ is a strongly electrophilic species. Therefore, the HOMO located at the benzene ring of BA seemed to easily receive electrophilic attacks from these ROS. Fig. 11(d) also illustrates the electrostatic potential (ESP)-mapped isosurface of BA, which also indicates that the electron-rich region (the blue-colored zones) of BA would be prone to electrophilic reactions.

For distinguishing the probable portion of BA for gaining attacks, the Fukui indices of BA were then computed and listed in Fig. 11(e). In particular, f^-, f^0, and f^+ represent the electrophilic attack, the radical attack, and the nucleophilic attack, respectively. Since $^1O_2$ is a highly reactive electrophilic species, sites of BA with relatively high and positive values of f^- would tend to receive the electrophilic attacks. Specifically, O1, O2, C14, and C15 have relatively high f- values, suggesting that these sites might undergo the electrophilic attacks. However, since O1 and O2 would be in saturation, C14 and C15 were even more possible

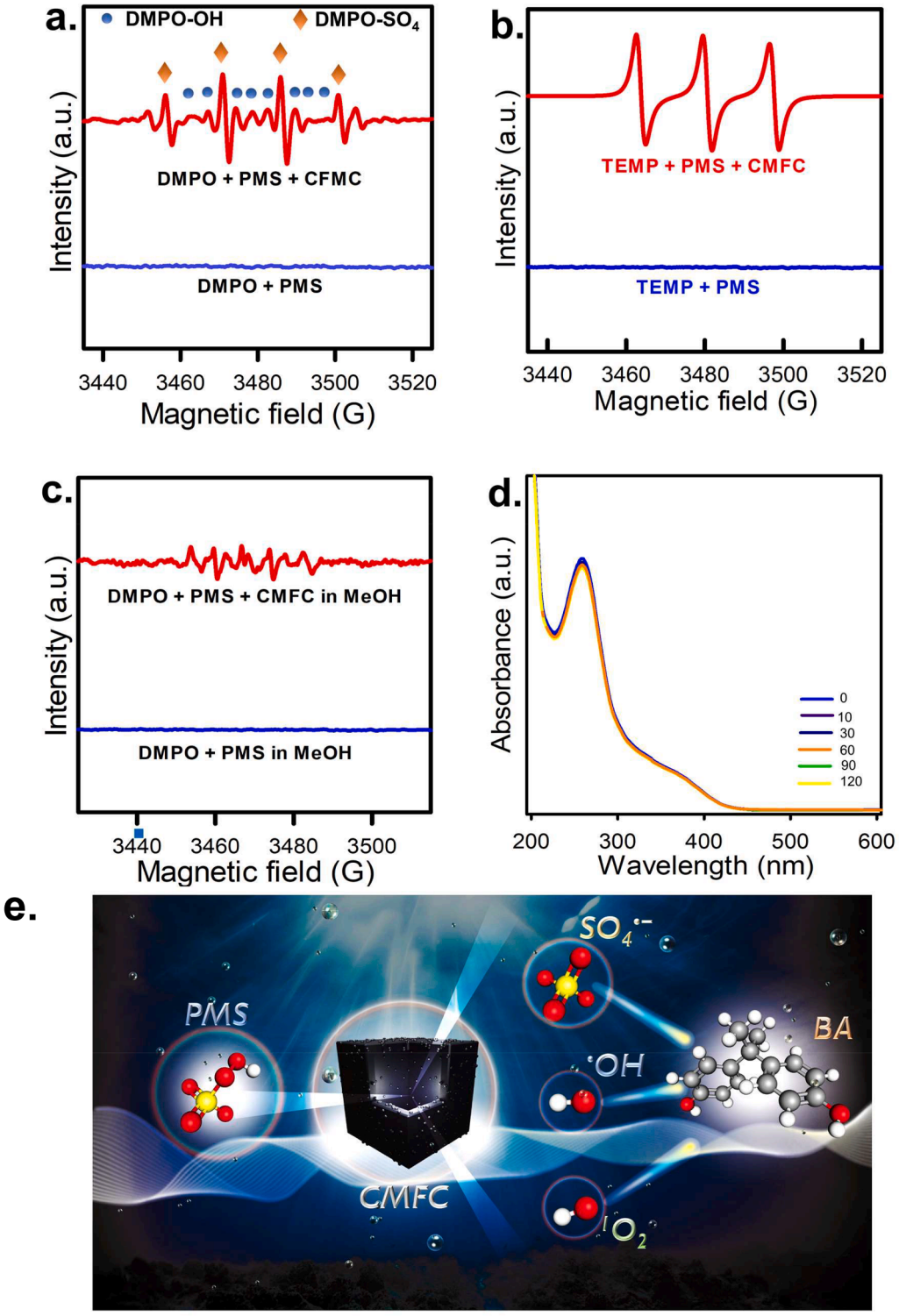

Fig. 10. EPR analyses: (a) DMPO, (b) TEMP, (c) DMPO in methanol; (d) Determination of superoxide by the NBT test; (e) illustration of the mechanism of BA degradation.

sites to accept initial attacks. Beside, the sites with high values of f^0 would tend to receive the radical attacks; similarly, C14, and C15 might be more susceptible to radical attacks during BA degradation by CMFC+PMS.

To determine the decomposition pathway of BA by CMFC+PMS, the mass spectrometry of decomposition products from BA degradation (Fig. S9 and Table S3) was then analyzed and combined with the above-mentioned theoretical knowledge to propose the degradation process in Fig. 12. In the beginning, the benzene ring(s) of BA might be substituted by an OH to form initial intermediates, P1 and P2. Subsequently, P1 and P2 might be further attacked to undergo ring-opening reactions, forming P3. Next, P3 might be continuously decomposed to afford P4, which could be then degraded to generate P5. Upon more attacks, P5 would then undergo another ring-opening reaction to afford P6 as well as P7. The two by-products might be then decomposed to produce a series of smaller compounds, such as P8, and then P9. These intermediates would

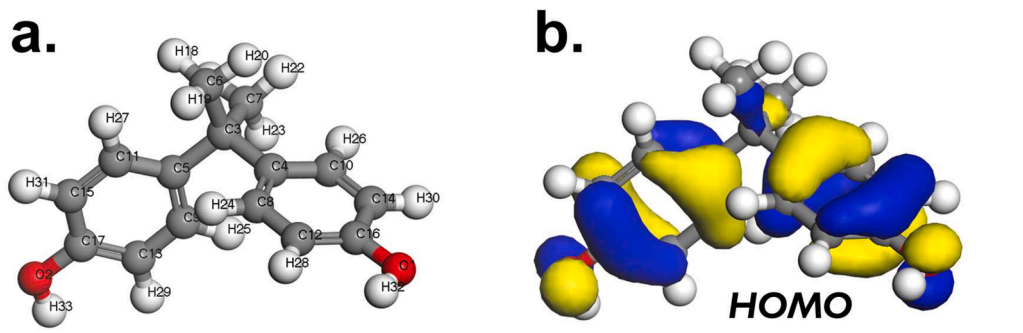

e.

ATOM	Number	Fukui(-)	Fukui(0)	Fukui(+)
O	1	**0.079**	**0.057**	0.036
O	2	**0.079**	**0.058**	0.037
C	3	-0.013	-0.014	-0.015
C	4	0.01	0.004	-0.002
C	5	0.022	0.004	-0.013
C	6	-0.014	-0.016	-0.019
C	7	-0.011	-0.017	-0.023
C	8	0.016	0.031	0.046
C	9	0.015	0.031	0.047
C	10	0.02	0.03	0.04
C	11	0.017	0.03	0.044
C	12	0.028	0.037	0.046
C	13	0.029	0.037	0.045
C	14	**0.037**	**0.047**	0.058
C	15	**0.033**	**0.047**	0.061
C	16	0.028	0.021	0.014
C	17	0.029	0.021	0.014

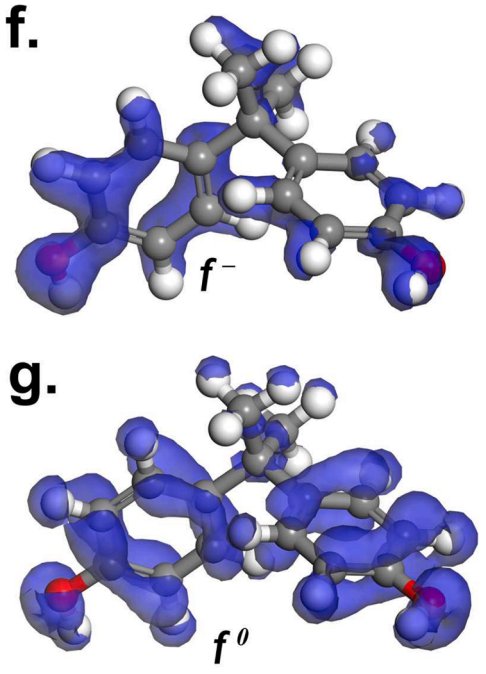

Fig. 11. DFT calculation for BA: (a) the optimized molecule structure, (b) HOMO; (c) LUMO, (d) electrostatic potential (ESP); (e) a summary of Fukui indices; condensed Fukui index distribution for (f) electrophilic attack (f^-), and (g) radical attack (f^0).

eventually be decomposed to become H_2O and CO_2.

3.7. Eco-toxicity evaluation of BA degradation intermediates

Based on the decomposition process of BA by CMFC+PMS, it was also crucial to evaluate the eco-toxicity of intermediates generated from BA elimination particularly for aquatic ecology. Herein, the Ecological Structure Activity Relationships (ECOSAR) Predictive Model is then adopted here to examine variations in toxicity of degradation intermediates from BA based on acute toxicity ($LC50_{fish/daphnia}$ & $EC50_{green\ algae}$) and chronic toxicity ($ChV_{fish/daphnia/green\ algae}$) as shown in Fig. 13(a) and (b), respectively. Based on the Globally Harmonized System of Classification and Labeling of Chemicals (Table S4), the data of LC50 of these intermediates from the ECOSAR could be then categorized into the four levels of toxicity (i.e., very toxic, toxic, harmful and non-harmful). Fig. 13(b) displays values of Log LC50 of these intermediates as well as their categories. In the case of daphnia magna, the toxicity of pristine BA was relatively high (i.e., very low dosage of LC50). As BA was decomposed, the toxicities of the initial intermediates (P1 and P2) seemed to decrease gradually, and then toxicities were significantly reduced in P3–P9.

Similarly, the same tendency was also observed in the case of fathead

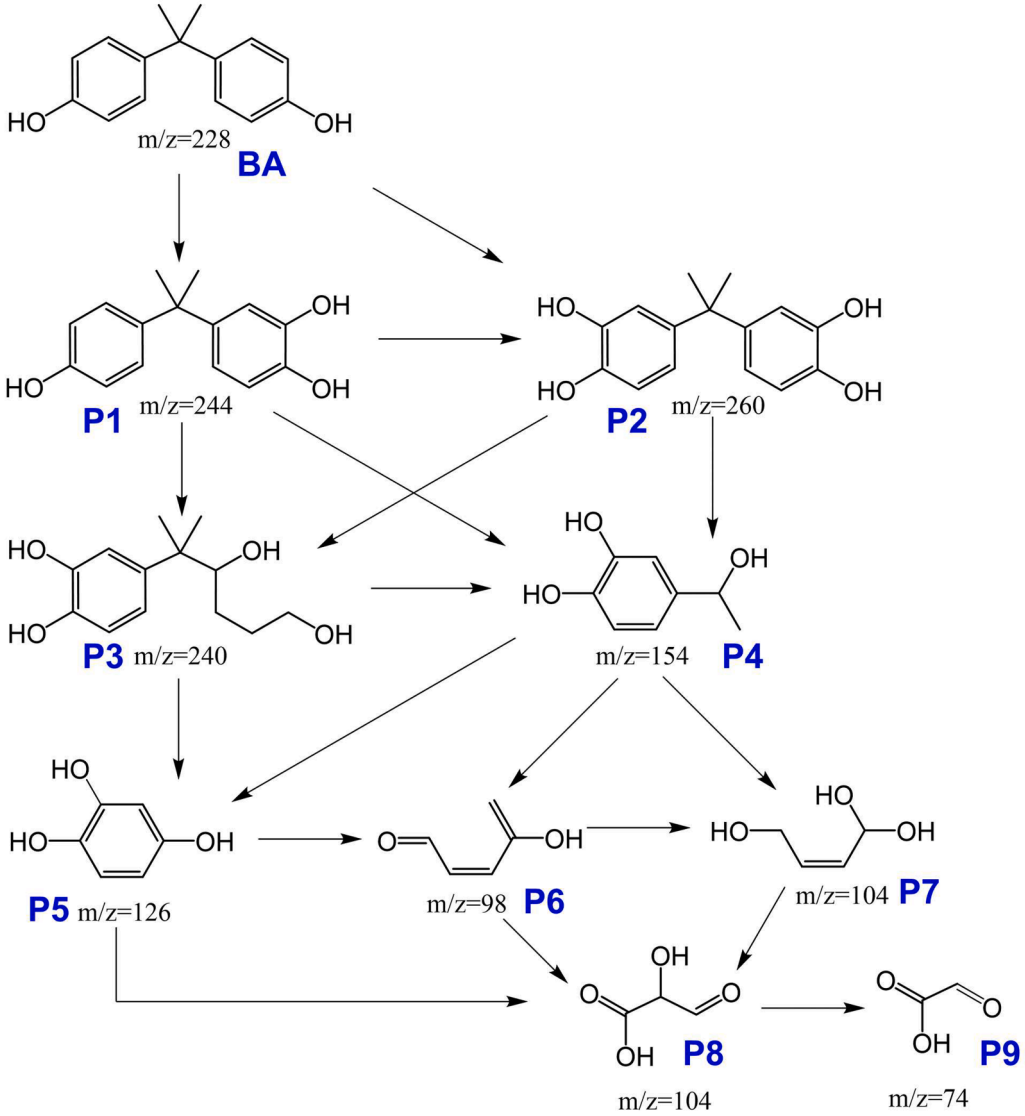

Fig. 12. A proposed degradation process of BA based on the detected intermediates.

minnow as the initial toxicity of BA was high, and gradually decreased along the decomposition process. These results suggest that while BA could be considered as a harmful chemical, its degradation intermediates by CMFC+PMS were mostly non-harmful, demonstrating that CMFC+PMS was useful to degrade BA without the occurrence of toxic/very toxic intermediates, and also detoxify BA along the decomposition. Furthermore, the bioconcentration factors (BCF) of these degradation intermediates were also evaluated by using the Toxicity Estimation Software Tool from U.S. Environmental Protection Agency for elucidating the variation of bioaccumulation tendencies of BA and its degradation intermediates. Fig. 13(c) shows that initially, BCF exhibits a very high BCF, which would be slightly decreased once BA was degraded to become P1. Subsequently, when P1 was further degraded to P2 and then P3, their corresponding BCF were substantially reduced. On the other hand, BCF of other degradation intermediates also became much lower than that of BA, indicating that CMFC+PMS successfully degraded BA and also reduced toxicities and environmental impact of BA.

4. Conclusion

For developing a useful heterogeneous catalyst to activate PMS, herein, CMFC was proposed and successfully fabricated here to exhibit a unique hollow-engineered nanostructure and the composition of FeCo alloy by using Co-ZIF as a precursor after the facile etching and Fe doping treatments. The Fe dopant embedded FeCo alloy NPs into the hollow-structured N-doped carbon matrix, enabling CMFC to possess the higher meso-porosity, active N species as well as more superior electrochemical properties than its analogue without Fe dopants, CMC. Thus, CMFC exhibited a considerably larger activity than CMC and the benchmark catalyst, Co_3O_4 NP, for PMS activation to degrade BA. Beside, CMFC+PMS showed an even lower E_a for BA degradation than literatures, and retained its high efficiency for eliminating BA in different water media. CMFC also maintained its composition and activities over multiple degradation cycles. CMFC also exhibited a high saturation magnetization, making it magnetically-controllable. The mechanism of BA decomposition has been thoroughly investigated and radical and non-radical routes have been revealed. In accordance to the ecotoxicity assessment, BA degradation by CMFC+PMS did not result in the formation of toxic and extremely toxic byproducts during its decomposition process. This makes CMFC a promising heterogeneous catalyst for PMS activation to degrade BA and other refractory contaminants in water.

CRediT authorship contribution statement

Tran Doan Trang: Data curation, Writing – original draft. **Ta Cong**

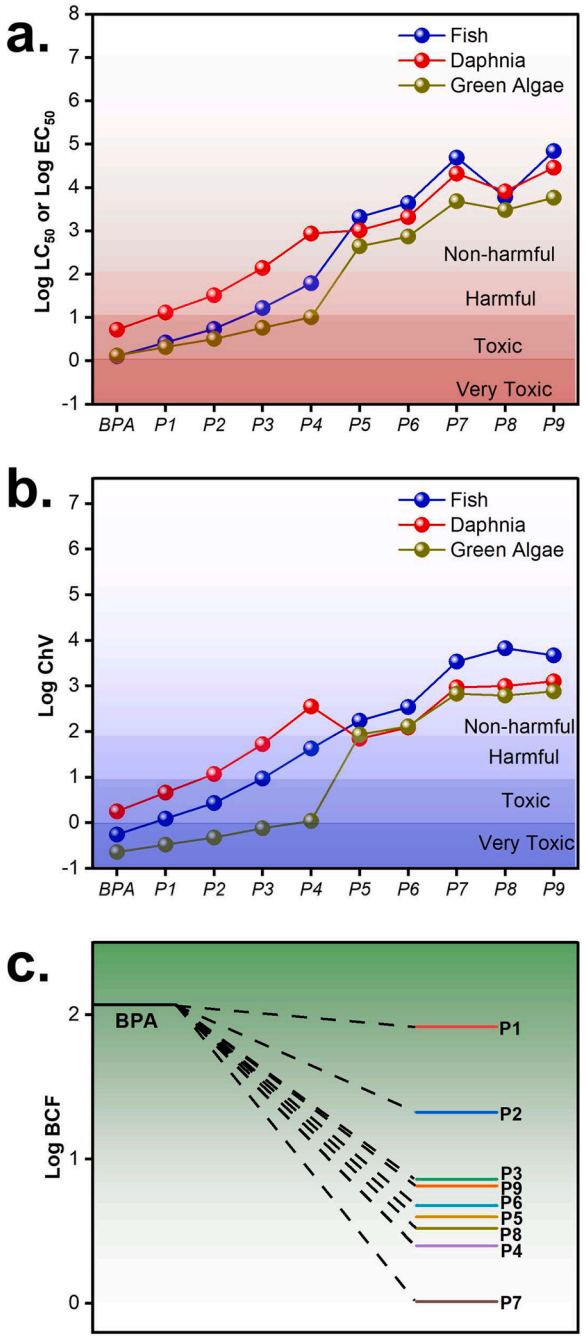

Fig. 13. Eco-toxicity evaluation by the ECOSAR, and the Toxicity Estimation Software Tool (a) acute toxicities; (b) chronic toxicities; and (c) bio-concentration factor (BCF).

Khiem: Data curation, Conceptualization. **Eilhann Kwon:** Writing – original draft. **Jet-Chau Wen:** Data curation, Visualization, Investigation. **Xiaoguang Duan:** Writing – review & editing. **Ha Manh Bui:** Data curation. **Chechia Hu:** Writing – original draft. **Yiu Fai Tsang:** Visualization. **Wei-Hsin Chen:** Investigation. **Kun-Yi Andrew Lin:** Writing – original draft.

Declaration of Competing Interest

The authors declare that they have no known competing financial interests or personal relationships that could have appeared to influence the work reported in this paper.

Data availability

Data will be made available on request.

Supplementary materials

Supplementary material associated with this article can be found, in the online version, at doi:10.1016/j.surfin.2023.103338.

References

[1] Z.Y. Choong, M.F. Gasim, K.Y.A. Lin, T.S. Hamidon, H. Hussin, W.D. Oh, Unravelling the formation mechanism and performance of nitrogen, sulfur codoped biochar as peroxymonosulfate activator for gatifloxacin removal, Chem. Eng. J. 451 (2023), 138958.
[2] Z.Y. Choong, K.Y.A. Lin, G. Lisak, T.T. Lim, W.D. Oh, Multi-heteroatom-doped carbocatalyst as peroxymonosulfate and peroxydisulfate activator for water purification: a critical review, J. Hazard. Mater. 426 (2022) 128077.
[3] S. Giannakis, K.Y.A. Lin, F. Ghanbari, A review of the recent advances on the treatment of industrial wastewaters by Sulfate Radical-based Advanced Oxidation Processes (SR-AOPs), Chem. Eng. J. 406 (2021), 127083.
[4] Q. Chen, Y. Liu, Y. Lu, Y. Hou, X. Zhang, W. Shi, Y. Huang, Atomically dispersed Fe/Bi dual active sites single-atom nanozymes for cascade catalysis and peroxymonosulfate activation to degrade dyes, J. Hazard. Mater. 422 (2022), 126929.
[5] W.J. Liu, Y.K. Park, H.M. Bui, N.N. Huy, C.H. Lin, S. Ghotekar, T. Wi-Afedzi, K.Y. A. Lin, Hofmann-MOF-derived CoFeNi nanoalloy@ CNT as a magnetic activator for peroxymonosulfate to degrade benzophenone-1 in water, J. Alloy. Compd. 937 (2022) 165189.
[6] W.J. Liu, E. Kwon, B.X. Thanh, J. Lee, C.K. Ta, S. Sirivithayapakorn, K.Y.A. Lin, Nanoscale CoNi alloy@ carbon derived from Hofmann-MOF as a magnetic/ effective activator for monopersulfate to eliminate an ultraviolet filter, J. Nanostruct. Chem. (2022) 1–14.
[7] F. Li, H. Xia, Q.Q. Ni, Co, Ni-coordinated ZIF derived nitrogen doped carbon network with encapsulated alloy for microwave absorption, Diam. Relat. Mater. 120 (2021), 108669.
[8] L. Chang, X. Xie, X. Zhang, H. Chai, Y. Huang, Overlooked key role of Mo(VI) in Fe2 (MoO4)3 for peroxymonosulfate activation with 1O2 dominated degradation pathway, Sep. Purif. Technol. 322 (2023), 124360.
[9] Y. Zhou, Y. Zhang, X. Hu, Synergistic coupling Co3Fe7 alloy and CoFe2O4 spinel for highly efficient removal of 2,4-dichlorophenol by activating peroxymonosulfate, Chemosphere 242 (2020), 125244.
[10] W.J. Liu, E. Kwon, B. Xuan Thanh, T. Cong Khiem, D. Dinh Tuan, J.Y. Lin, T. Wi-Afedzi, C. Hu, S. Sirivithayapakorn, K.Y.A. Lin, Hofmann-MOF derived nanoball assembled by FeNi alloy confined in carbon nanotubes as a magnetic catalyst for activating peroxydisulfate to degrade an ionic liquid, Sep. Purif. Technol. 295 (2022), 120945.
[11] J. Sheng, S. Guo, C. Yuan, X. Nie, P. Cui, H. Jiang, Degradation bensulfuron-methyl by magnetic CoFe alloy@N-doped graphitized carbon derived from CoFe2O4 activated by peroxymonosulfate, Chem. Eng. J. 466 (2023), 143158.
[12] X. Sun, H. Qi, S. Mao, Z. Sun, Atrazine removal by peroxymonosulfate activated with magnetic CoFe alloy@N-doped graphitic carbon encapsulated in chitosan carbonized microspheres, Chem. Eng. J. 423 (2021), 130169.
[13] L. Hu, R. Zhang, L. Wei, F. Zhang, Q. Chen, Synthesis of FeCo nanocrystals encapsulated in nitrogen-doped graphene layers for use as highly efficient catalysts for reduction reactions, Nanoscale 7 (2015) 450–454.
[14] X. Zhu, Y. Zhang, S. Zhang, S. Yang, Q. Xu, Synthesis of magnetic FeCo/BC composite by one-step pyrolysis for degradation of bisphenol A through peroxymonosulfate/peroxydisulfate activization, J. Alloy. Compd. 924 (2022), 166500.
[15] P. Shukla, H. Sun, S. Wang, H.M. Ang, M.O. Tadé, Nanosized Co3O4/SiO2 for heterogeneous oxidation of phenolic contaminants in waste water, Sep. Purif. Technol. 77 (2011) 230–236.
[16] Y. Yao, Z. Yang, H. Sun, S. Wang, Hydrothermal synthesis of Co3O4–Graphene for heterogeneous activation of peroxymonosulfate for decomposition of phenol, Ind. Eng. Chem. Res. 51 (2012) 14958–14965.
[17] W.J. Ma, N. Wang, Y.C. Du, T.Z. Tong, L.J. Zhang, K.Y.A. Lin, X.J. Han, One-step synthesis of novel Fe3C@nitrogen-doped carbon nanotubes/graphene nanosheets for catalytic degradation of Bisphenol A in the presence of peroxymonosulfate, Chem. Eng. J. 356 (2019) 1022–1031.
[18] N. Wang, W.J. Ma, Z.Q. Ren, Y.C. Du, P. Xu, X.J. Han, Prussian blue analogues derived porous nitrogen-doped carbon microspheres as high-performance metal-free peroxymonosulfate activators for non-radical-dominated degradation of organic pollutants, J. Mater. Chem. A 6 (2018) 884–895.
[19] D.D. Tuan, W.D. Oh, F. Ghanbari, G. Lisak, S.P. Tong, K.Y.A. Lin, Coordination polymer-derived cobalt-embedded and N/S-doped carbon nanosheet with a hexagonal core-shell nanostructure as an efficient catalyst for activation of oxone in water, J. Colloid Interface Sci. 579 (2020) 109–118.
[20] H. Nguyen, J. Lee, E. Kwon, G. Lisak, B.X. Thanh, F. Ghanbari, K.Y.A. Lin, Bamboo-like N-doped carbon nanotube-confined cobalt as an efficient and robust catalyst

for activating monopersulfate to degrade bisphenol A, Chemosphere 279 (2021) 130569.
[21] X.G. Duan, H.Q. Sun, Y.X. Wang, J. Kang, S.B. Wang, N-doping-induced nonradical reaction on single-walled carbon nanotubes for catalytic phenol oxidation, ACS Catal. 5 (2015) 553–559.
[22] G. Zhou, L. Zhou, H. Sun, H.M. Ang, M.O. Tadé, S. Wang, Carbon microspheres supported cobalt catalysts for phenol oxidation with peroxymonosulfate, Chem. Eng. Res. Des. 101 (2015) 15–21.
[23] S. Wu, J. Liu, H. Wang, H. Yan, A review of performance optimization of MOF-derived metal oxide as electrode materials for supercapacitors, Int. J. Energy Res. 43 (2019) 697–716.
[24] X.W. Zhang, M.Y. Lan, F. Wang, C.C. Wang, P. Wang, C. Ge, W. Liu, Immobilized N-C/Co derived from ZIF-67 as PS-AOP catalyst for effective tetracycline matrix elimination: from batch to continuous process, Chem. Eng. J. 450 (2022), 138082.
[25] J.Y. Lin, J. Lee, W.D. Oh, E. Kwon, Y.C. Tsai, G. Lisak, S. Phattarapattamawong, C. Hu, K.Y.A. Lin, Hierarchical ZIF-decorated nanoflower-covered 3-dimensional foam for enhanced catalytic reduction of nitrogen-containing contaminants, J. Colloid Interface Sci. 602 (2021) 95–104.
[26] K.Y.A. Lin, W.D. Lee, Self-assembled magnetic graphene supported ZIF-67 as a recoverable and efficient adsorbent for benzotriazole, Chem. Eng. J. 284 (2016) 1017–1027.
[27] K.Y.A. Lin, H.A. Chang, Zeolitic Imidazole Framework-67 (ZIF-67) as a heterogeneous catalyst to activate peroxymonosulfate for degradation of Rhodamine B in water, J. Taiwan Inst. Chem. Eng. 53 (2015) 40–45.
[28] K.Y.A. Lin, Z.Y. Zhang, Degradation of Bisphenol A using peroxymonosulfate activated by one-step prepared sulfur-doped carbon nitride as a metal-free heterogeneous catalyst, Chem. Eng. J. 313 (2017) 1320–1327.
[29] H. Hu, B.Y. Guan, X.W. Lou, Construction of complex CoS hollow structures with enhanced electrochemical properties for hybrid supercapacitors, Chem 1 (2016) 102–113.
[30] C. Zhu, Y. Zhang, Z. Fan, F. Liu, A. Li, Carbonate-enhanced catalytic activity and stability of Co3O4 nanowires for 1O2-driven bisphenol A degradation via peroxymonosulfate activation: critical roles of electron and proton acceptors, J. Hazard. Mater. 393 (2020), 122395.
[31] X.Y. Jiang, E. Kwon, H.C. Chang, N.N. Huy, X. Duan, S. Ghotekar, Y.C. Tsai, A. Ebrahimi, F. Ghanbari, K.Y.Andrew Lin, Tuning nanostructured CuCo2O4 on 3D macro-support for enhanced degradation of carbofuran via catalytic activation monopersulfate: key roles of morphology and active species, Sep. Purif. Technol. 308 (2023), 122789.
[32] T.C. Khiem, N.N. Huy, E. Kwon, X. Duan, S. Wacławek, J. Bedia, Y.C. Tsai, A. Ebrahimi, F. Ghanbari, K.Y.A. Lin, Hetero-interface-engineered sulfur vacancy and oxygen doping in hollow Co9S8/Fe7S8 nanospheres towards monopersulfate activation for boosting intrinsic electron transfer in paracetamol degradation, Appl. Catal. B 330 (2023), 122550.
[33] T.C. Khiem, N.N. Huy, T.D. Trang, J.C. Wen, E. Kwon, H.C. Chang, C. Hu, X. Duan, K.Y.A. Lin, Boosting elimination of sunscreen, Tetrahydroxybenzophenone (BP-2), from water using monopersulfate activated by thorny NanoBox of Co@C prepared via the engineered etching strategy: a comparative and mechanistic investigation, Chemosphere 327 (2023), 138469.
[34] W.J. Liu, Y.K. Park, H.M. Bui, N.N. Huy, C.H. Lin, S. Ghotekar, T. Wi-Afedzi, K.Y. A. Lin, Hofmann-MOF-derived CoFeNi nanoalloy@CNT as a magnetic activator for peroxymonosulfate to degrade benzophenone-1 in water, J. Alloy. Compd. 937 (2023), 165189.
[35] D.D. Tuan, K.Y.A. Lin, Ruthenium supported on ZIF-67 as an enhanced catalyst for hydrogen generation from hydrolysis of sodium borohydride, Chem. Eng. J. 351 (2018) 48–55.
[36] W.J. Liu, E. Kwon, N.N. Huy, T.C. Khiem, G. Lisak, T. Wi-Afedzi, C.C. Wu, F. Ghanbari, K.Y.A. Lin, Facilely-prepared sulfide-doped Co3O4 nanocomposite as a boosted catalyst for activating Oxone to degrade a sunscreen agent, J. Taiwan Inst. Chem. Eng. 133 (2022), 104253.
[37] G. Li, J.H. Sun, W.P. Hou, S.D. Jiang, Y. Huang, J.X. Geng, Three-dimensional porous carbon composites containing high sulfur nanoparticle content for high-performance lithium-sulfur batteries, Nat. Commun. 7 (2016) 10601.
[38] Z. Hasan, D.W. Cho, C.M. Chon, K. Yoon, H. Song, Reduction of p-nitrophenol by magnetic Co-carbon composites derived from metal organic frameworks, Chem. Eng. J. 298 (2016) 183–190.
[39] P. He, Y. Wu, H. Chen, Z. Zhu, H. Liu, J. Gao, H. Xu, Hierarchical bimetal embedded in carbon nanoflower electrocatalysts derived from metal-organic frameworks for efficient oxygen evolution reaction, J. Alloy. Compd. 813 (2020), 152192.
[40] D.Y. Osadchii, A.I. Olivos-Suarez, A.V. Bavykina, J. Gascon, Revisiting nitrogen species in covalent triazine frameworks, Langmuir 33 (2017) 14278–14285.
[41] Z. Liu, X. Sun, Z. Sun, CoNi alloy anchored onto N-doped porous carbon for the removal of sulfamethoxazole: catalyst, mechanism, toxicity analysis, and application, Chemosphere 308 (2022), 136291.
[42] J. Miao, W. Geng, P.J.J. Alvarez, M. Long, 2D N-doped porous carbon derived from polydopamine-coated graphitic carbon nitride for efficient nonradical activation of peroxymonosulfate, Environ. Sci. Technol. 54 (2020) 8473–8481.
[43] Y. Wang, X. Wei, X. Hu, W. Zhou, Y. Zhao, Effect of Formic Acid Treatment on the Structure and Catalytic Activity of Co3O4 for N2O Decomposition, Catal. Lett. 149 (2019) 1026–1036.
[44] Z. Wang, W. Wang, L. Zhang, D. Jiang, Surface oxygen vacancies on Co3O4 mediated catalytic formaldehyde oxidation at room temperature, Catal. Sci. Technol. 6 (2016) 3845–3853.
[45] D.I.T. Oyekunle, B.B. Wu, F. Luo, J. Ali, Z.Q. Chen, Synergistic effects of Co and N doped on graphitic carbon as an *in situ* surface-bound radical generation for the rapid degradation of emerging contaminants, Chem. Eng. J. 421 (2021) 129818.
[46] T. Zeng, H.Y. Zhang, Z.Q. He, J.M. Chen, S. Song, Mussel-inspired approach to constructing robust cobalt-embedded N-doped carbon nanosheet toward enhanced sulphate radical-based oxidation, Sci. Rep. 6 (2016), 33348.
[47] S. Qu, Y. Yuan, X. Yang, H. Xu, A.K. Mohamed, J. Zhang, C. Zhao, L. Liu, B. Wang, X. Wang, J. Rinklebe, Y.C. Li, S. Wang, Carbon defects in biochar facilitated nitrogen doping: the significant role of pyridinic nitrogen in peroxymonosulfate activation and ciprofloxacin degradation, Chem. Eng. J. 441 (2022), 135864.
[48] T. Cong Khiem, X. Duan, W.J. Liu, Y.K. Park, H. Manh Bui, W.D. Oh, S. Ghotekar, Y. Fai Tsang, K.Y. Andrew Lin, MOF-templated hollow cobalt sulfide as an enhanced oxone activator for degradation of UV absorber: key role of sulfur vacancy-induced highly active CoII sites, Chem. Eng. J. 453 (2022) 139699.
[49] Y. Li, F.M. Li, X.Y. Meng, S.N. Li, J.H. Zeng, Y. Chen, Ultrathin Co3O4 nanomeshes for the oxygen evolution reaction, ACS Catal. 8 (2018) 1913–1920.
[50] J. Choi, M. Cui, Y. Lee, J. Kim, Y. Son, J. Khim, Hydrodynamic cavitation and activated persulfate oxidation for degradation of bisphenol A: kinetics and mechanism, Chem. Eng. J. 338 (2018) 323–332.
[51] T. Olmez-Hanci, I. Arslan-Alaton, B. Genc, Bisphenol A treatment by the hot persulfate process: oxidation products and acute toxicity, J. Hazard. Mater. 263 (2013) 283–290.
[52] A. Ghauch, A.M. Tuqan, Oxidation of bisoprolol in heated persulfate/H2O systems: kinetics and products, Chem. Eng. J. 183 (2012) 162–171.
[53] B. Yan, H. Deng, H. Wei, L. Chen, H. Liu, T. Song, X. Yu, Performance and kinetics of BPA degradation initiated by powdered iron (or ferrous sulfate) and persulfate in aqueous solutions, Catalysts 13 (2023) 36.
[54] H.T. Nguyen, J. Lee, E. Kwon, G. Lisak, B.X. Thanh, W.D. Oh, K.Y.A. Lin, Metal-complexed covalent organic frameworks derived N-doped carbon nanobubble–embedded cobalt nanoparticle as a magnetic and efficient catalyst for oxone activation, J. Colloid Interface Sci. 591 (2021) 161–172.
[55] D.D. Tuan, E. Kwon, S. Phattarapattamawong, B.X. Thanh, T.C. Khiem, G. Lisak, H. Wang, K.Y.A. Lin, Nitrogen-containing carbon hollow nanocube-confined cobalt nanoparticle as a magnetic and efficient catalyst for activating monopersulfate to degrade a UV filter in water, J. Environ. Chem. Eng. 10 (2022), 106989.
[56] W. Guo, S. Su, C. Yi, Z. Ma, Degradation of antibiotics amoxicillin by Co3O4-catalyzed peroxymonosulfate system, Environ. Prog. Sustain. Energy 32 (2013) 193–197.
[57] D.D. Tuan, C. Khiem, E. Kwon, Y.F. Tsang, S. Sirivithayapakorn, B.X. Thanh, G. Lisak, H. Yang, K.Y.A. Lin, Hollow porous cobalt oxide nanobox as an enhanced for activating monopersulfate to degrade 2-hydroxybenzoic acid in water, Chemosphere 294 (2022), 133441.
[58] T. Zhang, Y. Chen, Y. Wang, J.Le Roux, Y. Yang, J.P. Croué, Efficient peroxydisulfate activation process not relying on sulfate radical generation for water pollutant degradation, Environ. Sci. Technol. 48 (2014) 5868–5875.
[59] J.Y. Yin, H. Wang, K.P. Yu, J. Lee, K.Y.A. Lin, Degradation of sunscreen agent 2-phenylbenzimidazole-5-sulfonic acid using monopersulfate activated by MOF-derived cobalt sulfide nanoplates, J. Water Process Eng. 44 (2021), 102282.
[60] T.C. Khiem, D.D. Tuan, E. Kwon, N.N. Huy, W.D. Oh, W.H. Chen, K.Y.A. Lin, Degradation of dihydroxybenzophenone through monopersulfate activation over nanostructured cobalt ferrites with various morphologies: a comparative study, Chem. Eng. J. 450 (2022), 137798.
[61] T.C. Khiem, X. Duan, W.J. Liu, Y.K. Park, H.M. Bui, W.D. Oh, S. Ghotekar, Y. F. Tsang, K.Y.A. Lin, MOF-templated hollow cobalt sulfide as an enhanced Oxone activator for degradation of UV Absorber: key role of sulfur Vacancy-Induced highly active CoII sites, Chem. Eng. J. 453 (2023), 139699.
[62] S. Mostafa, F.L. Rosario-Ortiz, Singlet oxygen formation from wastewater organic matter, Environ. Sci. Technol. 47 (2013) 8179–8186.
[63] T.C. Khiem, P.H. Mao, Y.K. Park, X. Duan, B.X. Thanh, C. Hu, S. Ghotekar, Y. F. Tsang, K.Y.A. Lin, Templating agent-mediated Cobalt oxide encapsulated in Mesoporous silica as an efficient oxone activator for elimination of toxic anionic azo dye in water: mechanistic and DFT-assisted investigations, Chemosphere 313 (2023), 137309.
[64] T. Cong Khiem, D. Dinh Tuan, E. Kwon, N. Nhat Huy, W.D. Oh, W.H. Chen, K.Y. A. Lin, Degradation of dihydroxybenzophenone through monopersulfate activation over nanostructured cobalt ferrites with various morphologies: a comparative study, Chem. Eng. J. 450 (2022), 137798.